



저작자표시-비영리-변경금지 2.0 대한민국

이용자는 아래의 조건을 따르는 경우에 한하여 자유롭게

- 이 저작물을 복제, 배포, 전송, 전시, 공연 및 방송할 수 있습니다.

다음과 같은 조건을 따라야 합니다:



저작자표시. 귀하는 원저작자를 표시하여야 합니다.



비영리. 귀하는 이 저작물을 영리 목적으로 이용할 수 없습니다.



변경금지. 귀하는 이 저작물을 개작, 변형 또는 가공할 수 없습니다.

- 귀하는, 이 저작물의 재이용이나 배포의 경우, 이 저작물에 적용된 이용허락조건을 명확하게 나타내어야 합니다.
- 저작권자로부터 별도의 허가를 받으면 이러한 조건들은 적용되지 않습니다.

저작권법에 따른 이용자의 권리는 위의 내용에 의하여 영향을 받지 않습니다.

이것은 [이용허락규약\(Legal Code\)](#)을 이해하기 쉽게 요약한 것입니다.

[Disclaimer](#)

공학박사 학위논문

**Mechanism Studies of Titanium Dioxide and
Bismuth as Electrode Materials for
Lithium-Ion Batteries**

리튬이온전지를 위한 티타늄 산화물과 비스무스
전극 물질의 메커니즘 연구

2022년 8월

서울대학교 대학원
공과대학 화학생물공학부
김민섭

Mechanism Studies of Titanium Dioxide and Bismuth as Electrode Materials for Lithium-Ion Batteries

리튬이온전지를 위한 티타늄 산화물과 비스무스
전극 물질의 메커니즘 연구

지도 교수 성 영 은

이 논문을 공학박사 학위논문으로 제출함
2022년 8월

서울대학교 대학원
공과대학 화학생물공학부
김 민 섭

김민섭의 공학박사 학위논문을 인준함
2022년 8월

위 원 장 _____ (인)

부위원장 _____ (인)

위 원 _____ (인)

위 원 _____ (인)

위 원 _____ (인)

Abstract

Mechanism Studies of Titanium Dioxide and Bismuth as Electrode Materials for Lithium-Ion Batteries

Min-Seob Kim

School of Chemical and Biological Engineering

The Graduate School

Seoul National University

Lithium-ion batteries (LIBs) have been received worldwide attention with increasing demands for electric vehicles and electric devices owing to their long life spans and high energy density compared to other energy storage system. However, currently widely used graphite as anode material which has low theoretical (372 mAh g^{-1}) and volumetric capacity (840 mAh cm^{-3}) is unable to meet increased demands. In order to replace state of the art carbon-based materials, many researchers have extensively investigated alternative electrode materials under not only ordinary temperature but elevated temperature.

In chapter 1, we elucidate the general concept of LIBs to clearly understand the following chapter. More detailed, we introduce the overall chronological record of mechanism studies on anatase TiO_2 and trend of bismuth metal for LIBs

In chapter 2, the study is focused on the chemical and structural origin of Li-ion battery aging in mild thermal condition, using anatase TiO_2 as a model. LIBs usually are operated under $20 - 40 \text{ }^\circ\text{C}$ higher degrees than room temperature with heat

generation. Although macroscopic investigation of heat contribution has been proved to lead to degradation of battery performance, the molecular level structural and chemical origin under near-ambient temperature has not been elucidated. On the basis of the combined experiments of the electrochemical measurements, Cs-corrected electron microscopy and in situ analysis, we provide insights on battery performance under mild thermal conditions. Interestingly, mild thermal environment induces excess lithium storage even at 45 °C which is not detected at ordinary working temperature. Abnormal lithium intercalation enables sequential phase transition in anatase TiO₂ for the first few cycles, however, consequently leading to severe crystal cracking causing battery aging. Battery aging at a high working temperature is ubiquitous in all intercalation compounds, therefore, it is significant to understand the origin of battery aging for advanced battery electrode.

In chapter 3, micro/meso porous Bi@C nanoplates are synthesized by annealing Bi-MOFs (Metal Organic Frameworks) followed by microwave-assisted method to alleviate volume expansion and pulverization of anode materials during lithiation/delithiation process. The Bi@C nanoplates are composed of 10 – 50 nm sized Bi nanoparticles encapsulated in amorphous carbon shell. The electrode materials show superior cycle performance of high specific capacity (556 mAh g⁻¹) after 100 cycles at a current density of 100 mA g⁻¹. Moreover, Bi@C nanoplates exhibit excellent stable cycle performance, showing 200 mAh g⁻¹ after 1000 cycles even extremely high current density of 3000 mA g⁻¹. This outstanding performance of designed anode is due to nano-sized Bi and carbon shell which reduces the diffusion length of lithium ions and enhances the electrical conductivity of anode and suppress the pulverization and aggregation during cycling. Hierarchical micro/meso porous materials derived from Bi-MOF are a new type of nanostructure for engineering novel Bi-based anodes for LIBs.

Keywords: lithium-ion batteries, mechanism study, mild thermal condition, titanium dioxide, bismuth, metal organic frameworks

Student Number: 2017-25533

Table of Contents

Abstract	i
List of Tables	v
List of Figures.....	v
Chapter 1. Introduction	1
1.1. General introduction of lithium-ion batteries(LIBs)	1
1.2 Mechanism study on anatase titanium dioxide	5
1.3 Bismuth-based materials as an anode for lithium ion battery	8
1.4 References.....	11
Chapter 2. Operando Identification of the Chemical and Structural Origin of Li-Ion battery Aging at Near-Ambient Temperature	16
2.1. Introduction	16
2.2. Experimental	19
2.3. Results and discussion	21
2.4. Conclusion.....	56
2.5. References.....	57
Chapter 3. Bi-MOF Derived Micro/Meso-Porous Bi@C Nanoplates for High Performance Lithium-Ion Batteries	63
3.1. Introduction.....	63
3.2. Experimental	67
3.3. Results and Discussion	70
3.4. Conclusion	93
3.5. References.....	94
국문 초록.....	103
List of Publication.....	105

List of Tables

Chapter 3

Table 3.1.1 Comparison of Li storage performance on recent Bi@C composites

List of Figures

Chapter 1

Figure 1.1.1 A comparative study of battery discharge curves showing the variation of operating voltage vs. fraction of available capacity.⁵2

Figure 1.1.2 (a) Relative energy diagram of electrode potentials and electrolyte energy gap in LIBs; (b) schematic diagram of the lithium intercalation-de-intercalation reaction mechanism in a rechargeable lithium-ion battery containing solid electrodes and a liquid electrolyte.¹⁰4

Chapter 2

Figure 2.3.1. Representative TEM images of SiO₂@TiO₂@RF. 23

Figure 2.3.2. Representative TEM images of SiO₂@TiO₂@RF after calcination (750 °C, static air). RF polymers are removed after high temperature calcination. Amorphous TiO₂ layer crystallize into outer-shell comprising numerous 12 nm-sized anatase TiO₂ nanocrystals. 24

Figure 2.3.3. Low magnification TEM image of synthesized 12 NT after etching SiO₂ core. 25

Figure 2.3.4. High magnification TEM image (A, B) and selected area diffraction pattern (C) of synthesized 12 NT. 26

Figure 2.3.5. Representative FESEM image of 12NT. 27

Figure 2.3.6. XRD pattern of as-prepared 12 NT. 28

Figure 2.3.7. Electrochemical properties of anatase TiO₂ anodes. Voltage profiles of 12 NT during the initial discharge at a current density of 100 mA g⁻¹ at A) RT and B) 60 °C. Cyclic voltammograms of 12 NT at a scan rate of 0.1 mV s⁻¹ at C)

RT and D) 60 °C.....	30
Figure 2.3.8. (A) Voltage profile (current density of 100 mA g ⁻¹) and (B) cyclic voltammetry (scan rate of 0.1 mV s ⁻¹) of 12 NT at 45 °C.....	31
Figure 2.3.9. (A) Voltage profile (current density of 100 mA g ⁻¹) and (B) cyclic voltammetry (scan rate of 0.1 mV s ⁻¹) of 12 NT at 90 °C.....	32
Figure 2.3.10. <i>In situ</i> XRD analysis during the first cycle. A) Voltage profiles of 12 NT in the first cycle at RT (up) and 60 °C (down). Series of <i>in situ</i> XRD patterns for charge-discharge of 12 NT at B) RT and C) 60 °C in the first cycle. D) Schematic of crystal structure transformation of lithium intercalation on anatase TiO ₂ in RT and mild thermal condition (dotted box).	34
Figure 2.3.11. Custom-made <i>operando</i> heating XRD measurement setup.....	35
Figure 2.3.12. Crystal structure of anatase TiO ₂ during phase transition: (A) anatase TiO ₂ , (B) Li _{0.55} TiO ₂ and (C) Li ₁ TiO ₂	36
Figure 2.3.13. d values of the (101) planes (TiO ₂ and Li ₁ TiO ₂) and the (011) plane (Li _{0.55} TiO ₂) extracted from Figure 2.3.10.B and C (<i>in situ</i> XRD results).....	37
Figure 2.3.14. A) Voltage profiles of 12 NT at a current density of 100 mA g ⁻¹ in the 2 nd , 20 th , 40 th cycles at 60 °C. B) Capacity and ratio of region 1 and 2 in 12 NT in the 2 nd , 20 th , 40 th cycles at 60 °C.	39
Figure 2.3.15. A) Voltage profiles of anatase TiO ₂ at a current density of 100 mA g ⁻¹ in the 2 nd , 20 th , 40 th cycles at RT. B) Capacity and ratio of region 1 and 2 in anatase TiO ₂ in the 2 nd , 20 th , 40 th cycles at RT.....	40
Figure 2.3.16. A) Voltage profiles of anatase TiO ₂ at a current density of 100 mA g ⁻¹ in the 2 nd , 20 th , 40 th cycles at 90 °C. B) Capacity and ratio of region 1 and 2 in anatase TiO ₂ in the 2 nd , 20 th , 40 th cycles at 90 °C.....	41
Figure 2.3.17. <i>In situ</i> XRD analysis at prolonged cycles. A) Voltage profiles of 12 NT at 60 °C in 10 th cycle (up) and 20 th cycle (down). Series of <i>in situ</i> XRD patterns for charge-discharge of 12 NT at 60 °C in B) 10 th cycle and C) 20 th cycle.....	42
Figure 2.3.18. Representative Cs-corrected STEM images of 12 NT after the 20 th lithium intercalation cycle at 60 °C (point v in Figure 2.3.17.C). A) Low magnification and B) high magnification bright field (BF)-STEM image of cracked anatase TiO ₂ crystals after 20 th cycling. C) Higher magnified BF-STEM image of a region marked by square in Figure 2.3.18.B (scale bar, (A) 200 nm, (B) 20 nm, and (C) 10 nm). D) Schematic of battery aging through intra-crystal stress	

generation and subsequent crystal cracking during lithium intercalation in mild thermal condition.	44
Figure 2.3.19. Low magnification TEM and STEM images of 12 NT after the 20 th lithium intercalation cycle at 60 °C. Nanostructures are well preserved.	45
Figure 2.3.20. High magnification BF-STEM images of 12 NT after the 20 th lithium intercalation cycle at 60 °C. In A), a, b and c compose initial anatase TiO ₂ crystal. White dotted line guides abrupt crystal interface. c part is missing upon continuous cycling. For comparison, identical image is shown on B) without figure legends.	46
Figure 2.3.21. Cs-corrected BF-STEM images of 12 NT after the 20 th lithium intercalation cycle at RT.....	47
Figure 2.3.22. XRD patterns of 12 NT before the test and after the 1 st , 10 th and 20 th lithium intercalation cycle at 60 °C.....	48
Figure 2.3.23. XRD patterns of 12 NT before the test and after the 1 st , 10 th and 20 th lithium intercalation cycle at RT.....	49
Figure 2.3.24. Voltage profiles of 12 NT after (A) 1 st , (B) 2 nd , (C) 10 th and (D) 20 th lithium intercalation cycle at 60 °C. The irreversible Li loss accounts 30%, 13%, 8%, and 7% on the 1 st , 2 nd , 10 th , and 20 th cycle, respectively.	51
Figure 2.3.25. (A) Voltage profile comparison before and after the battery degradation (90 °C, 100 mA g ⁻¹), and (B) voltage profiles of the degraded electrode at different rates (90 °C, 100 mA g ⁻¹ , 50 mA g ⁻¹ , 25 mA g ⁻¹ , and 10 mA g ⁻¹). During the battery degradation, significant shortage of voltage plateau at 1.75 V is observed (A). The capacity in the lower voltage slope (region 2) was partially recovered under lower cycling rates, while capacity at 1.75 V plateau remained unchanged (B).....	53
Figure 2.3.26. A) Cycle performance of 12 NT at a current density of 100 mA g ⁻¹ at various temperature (RT, 60 °C, 90 °C). B) Cycle performance of 12 NT at 100 mA g ⁻¹ through thermal condition change from 60 °C to RT after 20 cycles.....	55

Chapter 3

Figure 3.3.1 Schematic illustration of preparation of Bi@C.....	71
Figure 3.3.2 The SEM images of Bi-MOF after microwave-assisted hydrothermal	

method	72
Figure 3.3.3 (a,b) SEM images of Bi@C after carbonization at different magnifications (c) N adsorption and desorption isotherm and (d) pore size distribution of Bi@C	73
Figure 3.3.4 (a-c) TEM images of Bi@C after carbonization at different magnifications (d) EDS images of Bi@C.....	75
Figure 3.3.5 (a) TEM images and (b) SAED patterns of Bi@C (scale bar = 10nm)	76
Figure 3.3.6 Weight ratio measurement analysis of Bi@C by TGA	77
Figure 3.3.7 XRD patterns of Bi@C	78
Figure 3.3.8 Electrochemical performance of the Bi@C (a) CV profiles of Bi@C for the first three cycles at a scan rate of 0.1 mV s ⁻¹ . (b) charge and discharge potential curves at 1,2,3,10,30,50 cycles. Lithium storage performance of the Bi@C and Bi commercial (c) cyclic performance at a current density of 100 mA g ⁻¹ . (d) C-rate performance at a current density of stepwise from 50 mA g ⁻¹ to 1000 mA g ⁻¹	79
Figure 3.3.9 Electrochemical performance of CV profiles of Bi commercial for the first three cycles at a scan rate of 0.1 mV s ⁻¹	81
Figure 3.3.10 Coulombic efficiency of Bi@C and Bi commercial calculated from Figure 3.3.8	82
Figure 3.3.11 Charge and discharge potential curves of Bi commercial at a current density of 100 mA g ⁻¹	83
Figure 3.3.12 The SEM images of Bi@C electrode (a) pristine (b) after 20 cycles and Bi commercial electrode (c) pristine (d) after 20 cycles (scale bar = 10μm)	85
Figure 3.3.13 <i>In situ</i> XRD patterns (left side) with voltage profiles (right side) of Bi@C and enlarged XRD patterns (center) between 20 and 30 degrees.....	87
Figure 3.3.14 Cycle performance of the Bi@C and Bi commercial (a) Cycle performance at a current density of 3000 mA g ⁻¹ . Charge and discharge potential curves of (b) Bi@C (c) Bi commercial at a current density of 3000 mA g ⁻¹	89
Figure 3.3.15 EIS analysis of Bi@C and Bi commercial measured after 100 cycles	91
Figure 3.3.16 (a,b) SEM images and (c) XRD patterns of Bi commercial	92

Chapter 1. Introduction

1.1. General introduction of lithium-ion batteries (LIBs)

As amount of energy usage has increased in various fields, much attention has been received to environmental energy. Conventionally used fossil fuel, non-sustainable renewable sources, faced limitations to reducing CO₂ emissions along with global warming. According to this trend, many studies have been actively researched on a variety of alternative energy sources such as solar cells, wind power and hydroelectric power which are environmentally eco-friendly renewable energy sources. Due to the unpredictable characteristics of this eco-friendly energy, interests on energy storage devices drastically increases. The battery is a device capable of easily portable energy carrier and static energy storage. Accordingly, studies on nickel cadmium, nickel metal hydride, lead acid battery and lithium ion batteries (LIBs) have been vigorously researched¹. Among them, the most promising LIBs for practical applications were initiated by SONY in 1990 introducing LiCoO₂ as a cathode and graphite as an anode.^{1,2} Compared to other conventional batteries mentioned before, LIBs have advantages of lightweight device, high operating voltage and highly stable performance.³ Fig. 1.1.1 shows the superiority of operating voltage rather than other batteries.⁴ Components of LIBs is divided into four main parts: anode, cathode, electrolyte and separator. As shown in Fig. 1.1.2.a, electrode is selected depending on not only electrochemical potential (μ_A for the anode and μ_C for the cathode) but relative HOMO-LUMO energy gap (E_g) of an electrolyte. To realize more stable battery performance, μ_A require lower energy than the electrolyte's LUMO, otherwise the electrolyte is reduced. On the contrary, oxidation of the electrolyte is prevented only when the oxidation of the electrolyte can be prevented only when μ_C is higher than the HOMO of the electrolyte. As mentioned above, firstly assembled LIBs is composed of graphite as an anode and LiCoO₂ as a cathode, and the two electrode are divided into porous permeable separator which

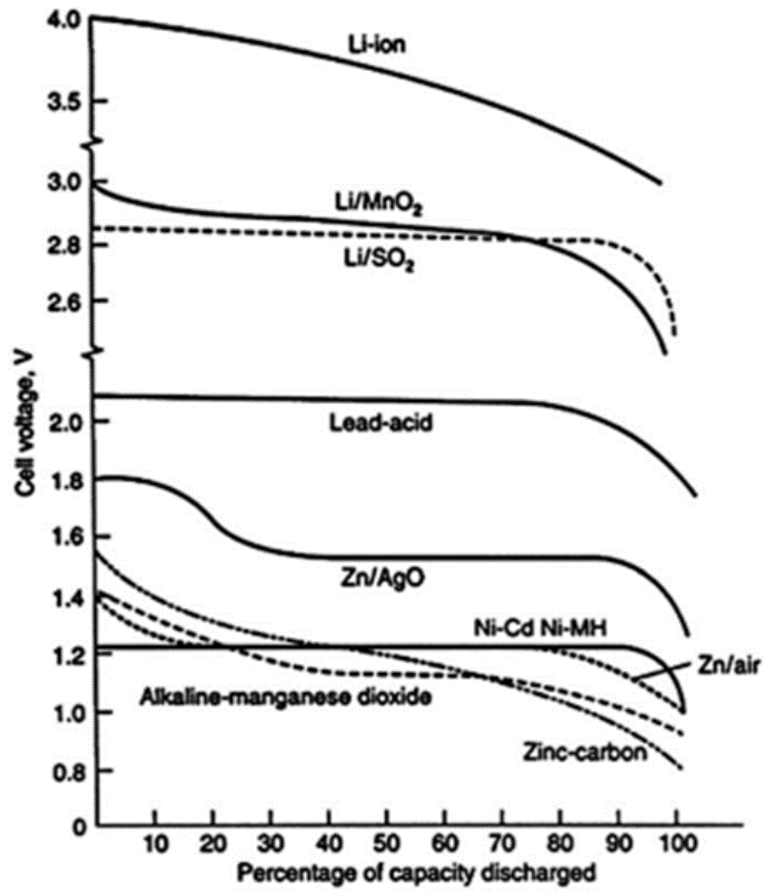


Figure 1.1.1 A comparative study of battery discharge curves showing the variation of operating voltage vs. fraction of available capacity.⁵

only allow lithium ions to transport but prevent a short circuit directly in contact with an electrode. Upon charging, lithium ions are extracted from the layered oxide cathode material, and the lithium ion is introduced into graphite which is a layered structure through an electrolyte. Fig. 1.1.2.b shows the mechanism of LIBs.



Electrons move through an external electrical circuit and couple with an additional positive charge in the electrode. On discharging, opposite mechanism occurs described above. Appropriate electrolyte is also essential in LIBs. Generally, the mixture of aprotic organic solvent with Li-salts is used as an electrolyte, such as ethylene carbonate (EC), propylene carbonates (PC), diethyl carbonate (DEC) mixed with hexafluorophosphate (LiPF_6) and lithium perchlorate (LiClO_4).⁶

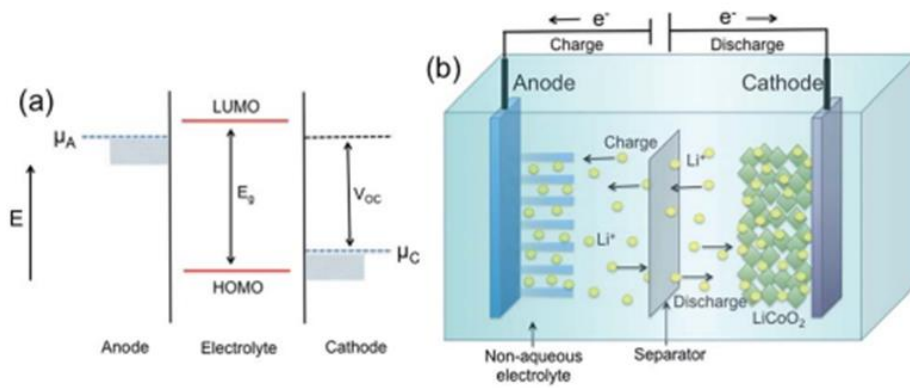
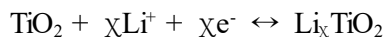


Figure 1.1.2 (a) Relative energy diagram of electrode potentials and electrolyte energy gap in LIBs; (b) schematic diagram of the lithium intercalation-deintercalation reaction mechanism in a rechargeable lithium-ion battery containing solid electrodes and a liquid electrolyte.⁴

1.2 Mechanism study on anatase titanium dioxide

Anatase TiO_2 is able to store lithium ions during electrochemical process. Within anatase TiO_2 phase, insertion/desertion of lithium ions are reserved at 1.4-1.8 V vs. Li/Li^+ following the reaction equation.¹



When anatase TiO_2 is used as an anode, similar to graphite, theoretical specific capacity of 335 mAh g^{-1} is obtained up to one lithium stored. This merit attracted much attention as an anode in LIBs. In addition, anatase phase can be synthesized more easily than other TiO_2 phase and is easy to engineer various nanostructure.

For these reasons, mechanism studies for properties of intercalated lithium ions in anatase TiO_2 have been extensively conducted. A new model has been proposed through first principal simulation for lithium storage in the anatase TiO_2 of the lithium intercalation mechanism.² The calculations demonstrated that lithium insertion was retarded by diffusion. Single phase reaction and intercalation was observed in the value of χ at range from 0.05 to 0.1 in $\text{Li}_\chi\text{TiO}_2$. Further proceeded, coexistence of lithium-rich and lithium-poor phase simultaneously existed and the lithium-rich phase is detected in the distorted orthorhombic phase in the form of $\text{Li}_{0.5}\text{TiO}_2$. The first principal calculations also revealed the lithiation mechanism of phase transition from tetragonal to orthorhombic in anatase TiO_2 .³ Primary mechanism is suggested that accommodation of donated charge in the $d(yz)$ orbitals in titanium to transform in orthorhombic phase which leads to Jahn-Teller distortion in lattice structure. A more in-depth model study was further researched by considering electronic state of pure anatase TiO_2 and hydrogenated titanate ($\text{H}_{0.5}\text{TiO}_2$) and sodium titanate ($\text{Na}_{0.5}\text{TiO}_2$). The stable structure of $\text{Li}_{0.5}\text{TiO}_2$ is proposed that it is induced from the similar ion radius of Li^+ and Ti^{3+} . ^7Li magic-angle-spinning nuclear magnetic resonance (MAS NMR) spectroscopy is introduced to study the

intercalated lithium and lithium ions in pristine anatase TiO_2 and orthorhombic lithiated titanate ($\text{Li}_{0.6}\text{TiO}_2$).⁴ The ^7Li solid state NMR spectroscopy confirmed that coexistence of lithium-rich phase and lithium-poor phase upon charging/discharging process. Through NMR spectroscopy, lithium hopping process in anatase and orthorhombic lithium titanate is accompanied with the activation energy of about 0.2 and 0.09 eV. In addition, with further evolved solid-state NMR, continuous lithium ion exchange was observed between lithium-rich and lithium-poor phases of lithium titanate from pristine anatase TiO_2 .⁵ Lithium ion flux is about $1.2 \times 10^{20} \text{ s}^{-1} \text{ m}^{-2}$ across the phase boundary. Furthermore, quasi-elastic neutron diffraction and force field molecular dynamics simulations was applied to investigate the configurations of localized lithium.⁶ Two apparent peaks were detected in the lithium-rich and lithium-poor phase in octahedral interstices. Intercalation sites in the distorted oxygen octahedra are existed distinctly where depends on the temperature to occupy octahedral interstices. Inserted lithium hops in the scale of picosecond between the two octahedral sites. Along the c-direction, short arrangement of lithium ions was detected. Besides, by *in situ* grazing incidence reflection mode X-ray absorption near edge structure (XANES) spectroscopy, near-surface structure of lithium in intercalated anatase TiO_2 was also investigated.⁷ In-depth and more detailed comprehensive understanding of lithium intercalation mechanism was revealed by a series of theoretical and lithiation studies.

With the rapid development of the nanostructured anatase TiO_2 anode, related mechanism studies have intensively investigated on lithium intercalation in nanoscale anatase materials. The reaction mechanism of lithiated anatase TiO_2 was unveiled on particle size effect.⁸ Different size of Li_xTiO_2 nanoparticles, were synthesized by chemical insertion of pure anatase nano-sized TiO_2 with n-butyllithium. Each particle size can be controlled by the amount of n-butyllithium corresponding to x value of 0, 0.12, 0.4, 0.8. This result confirmed that solubility of lithium-ion in various phases systematically depending on the nanoparticle size.

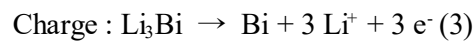
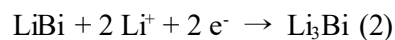
120 nm sized of anatase nanoparticles can accommodate $\text{Li/Ti} = 0.03$, on the other hand, 7 nm sized nano materials can up to $\text{Li/Ti} = 0.21$. In addition, electrochemical lithium intercalation leads to two phase reaction: coexistence of anatase/lithiated titanate(α/β) and lithiated titanate/ Li_xTiO_2 (β/γ). When lithium ions are inserted into anatase phase, drastic change of phase transition occurs in phase boundary. This study provided a comprehensive understanding of induced solid solution behavior between nanoparticles. Along with these studies, research on anatase TiO_2 anode materials has moved further into the nanoscale era. In LIBs system, the greatest advantages of nanostructured anode material is to shorten the diffusion path improving electrochemical performance. Pseudocapacitive effects, on the other hand, is another main contribution to capacity as the size of material was reduced to nanoscale. Pseudocapacitance occurs on the surface of electrode which endows fast and reversible redox reaction and it is fundamentally faradaic as compared to electric double layer capacitor.⁹ Pseudocapacitance appears on the surface and near-surface electrode indicating faradaic process. The contribution of pseudocapacitance according to the size of anatase TiO_2 was confirmed thorough detailed voltammetry analysis with the pure crystalline of anatase TiO_2 nanoparticles synthesized from nonhydrolytic sol-gel route.¹⁰ These results increase as the total stored charge and the capacitive contribution to the stored charge decrease in particle size. The contribution of capacitive part consists of a double layer and a pseudocapacitive effect. Furthermore, when the particle size decreases, the amount of charge from the lithium intercalation process decreases. This outcome is significant for the pseudo capacitive effect stored on the surface of TiO_2 to obtain high energy density.

Further than previous research, the charge-transfer process on the surface of nanosized anatase TiO_2 anode with hexafluorophosphate (LiPF_6) in ethylene carbonate(EC) and dimethyl carbonate (DMC) was confirmed by ^7Li NMR spectroscopy.¹¹ The consequence verifies the activation energy for diffusion of the electrode/electrolyte interface in the range of $10 - 25 \text{ kJ mol}^{-1}$ affecting the

composition of electrolyte. In addition, in-depth first principle of statistical method was used to study the kinetics and thermodynamics of anatase $\text{Li}_\chi\text{TiO}_2$.¹² As a result, thermodynamically stable phase at $\chi = 0.5$ can accommodate excess amount of lithium to vacant space up to $\chi = 0.6$ in $\text{Li}_\chi\text{TiO}_2$. Moreover, analytic results also found that within $\text{Li}_{0.5}\text{TiO}_2$, one-dimensional lithium ion diffusion path is parallel between anatase TiO_2 and $\text{Li}_{0.5}\text{TiO}_2$. In addition, lithium intercalation of structural changes in anatase nanotubes was identified by *in situ* Raman and *ex situ* powder neutron diffraction.¹³ This finding demonstrated that up to 0.98 lithium ions of anatase TiO_2 nanotubes can be stored per unit, and improved lithium storage capacity of anatase nanotubes can be obtained compared to bulk and other anatase nanoparticle.^{8, 14}

1.3 Bismuth-based materials as an anode for lithium ion battery

Metallic bismuth has the ability to store lithium ions under alloying process in which bismuth reacts with lithium ions following the reaction.^{1,2}



Bismuth metal has been considered to be an alternative materials due to high theoretical volumetric capacity (3800 mAh cm^{-3}) and suitable layered crystal structure (interlayer spacing along c-axis around 3.95 \AA).⁶ Tarascon's group firstly introduced bismuth metal as anode for rechargeable batteries in 2007 in which 10–20 nm sized bismuth nanoparticles were prepared by electrodeposition at room temperature showing possible capability as substitute for graphite.⁷ Omori et al. suggested a new method for spherical bismuth metal particles by annealing $70\text{B}_2\text{O}_3$ - $30\text{Bi}_2\text{O}_3$ glass in reduction as anode for LIBs.¹⁷ Besides, Liu et al. presented a 'top-

down' strategy to prepare bismuth nanorods from $\text{Al}_{30}\text{Bi}_{70}$ alloy ribbon via chemical dealloying achieving low charge transfer resistance (R_{ct}).⁸ This enhanced electrical conductivity could be ascribed to excellent performance of 301.9 mAh g^{-1} after 150 cycles.

Due to huge volume expansion during lithiation/delithiation process and poor conductivity of bismuth, it is an effective approach to coat bismuth particles with carbonaceous materials to improve electrochemical performance. Accordingly, Wang et al. synthesized porous Bi@C through one-step carbo thermal reduction (CTR) method.⁹ Porous carbon provides a conductive environment for electron transfer and alleviates volume expansion. Simultaneously, bismuth nanodots can effectively reduce a lithium ion diffusion path, thereby obtaining superior lithium storage performance of 520 mAh g^{-1} even after 100 cycles. Furthermore, Yuan et al. acquired egg-carton-inspired Bi@C composites by directly heat-treating bismuth citrate, where bismuth nanoparticles are compactly distributed on dense micro-sized 2D carbon frameworks.⁴ After delithiation, the electrode is returned to its original initial thickness inhibiting the drastic volume change of bismuth nanoparticles, which exhibiting long cycle stability (315 mAh g^{-1} at 1 A g^{-1} after 1000 cycles) of the Bi@C electrode and high volumetric capacity (1461 mAh cm^{-3} at 100 mA g^{-1}). With similar method, bismuth nanoparticle carbon composite has also been presented by Xiong et al.¹⁰ Bi@C composite in this article showed structure similar to that of the egg-carbon-inspired Bi@C composite above, resulting in surprisingly long-term cycle capacity (265 mAh g^{-1} at 8 A g^{-1} after 3000 cycles) and excellent rate rates (71 % retention at high current density of 60 A g^{-1}).

Zhang et al. synthesized a nitrogen-doped Bi@graphene compound based on the considerations that hetero atom doping can not only improves electrical conductivity but the electrochemical activity of carbon.³ Bismuth nanoparticles are tightly linked on N-Bi@graphene sheets. Substitution of carbon atom with nitrogen can derive much topological defects on graphene inducing more active sites for lithium ion

binding. Consequently, it showed superior rate performance at different current densities from 50 to 100 mA g⁻¹. Adopting the most common precursor, polydopamine (PDA), for nitrogen doping to carbon material, rose-like Bi@N-doped carbon nanocomposite was presented by Lan et al.¹ By optimizing the number of PDA coatings, Bi@N-48 exhibited outstanding specific capacity of 535 mAh g⁻¹ even after 450 cycles owing to synergistic effects including a flower-like structure with a large surface area and N-doped carbon with improved electrical conductivity and nanosized bismuth with shortened lithium ion diffusion path. Furthermore, Wang et al. introduced a new energy-efficient solution combustion synthesis (SCS) method to create 3D porous Bi@N-doped carbon composites.¹¹ Combustion synthesis type can effectively reduce resources consequently suitable for large scale industrial production.^{12, 13}

Metal-organic frameworks (MOFs) characterized by porosity, large surface area, various structures and metal types have been considered to be a highly promising precursor for designing nanostructures.¹⁴ Zhong et al. successfully applied Bi/NC compounds with carbonization of Zeolitic imidazolate framework (ZIF-8) and subsequently substitution of zinc to bismuth as an anode for LIBs.⁸⁸ Using Bi-BTC as a precursor for bismuth carbon composite, Chai et al. synthesized carbon-coated bismuth nano materials via facial reduction.² Interestingly, H₃BTC is not only an organic ligand of Bi-BTC, but also introduces as a carbon source in preparation process inhibiting new impurities. When used as an anode for LIBs, materials derived from Bi-MOF by above method can obtain excellent electrochemical performance and could provide a new way for bismuth electrode. Unlike closely connected core-shell structure, yolk-shell structure can effectively accommodate volume expansion with void space. Wang et al. elaborately designed bismuth nanorods which is surrounded by N-doped carbon nanotubes and synthesized by *in situ* thermal reduction of Bi₂S₃@polypyrrole nanorods with an excellent volumetric capacity of 1700 mAh cm⁻³ after 500 cycles.⁵

1.4 References

[1.1]

(1) Mizushima, K.; Jones, P. C.; Wiseman, P. J.; Goodenough, J. B. LiCoO_2 ($0 < x < 1$) : A New Cathode Material for Batteries of High Energy Density. *Mat. Res. Bull.* **1990**, *15*, 783.

(2) Yazami, R.; Touzain, P. H. A Reversible Graphite-Lithium Negative Electrode for Electrochemical Generators. *J. Power Sources*, **1983**, *9*, 365.

(3) Kim, M. -K.; Kim, M. -S.; Park, J. -H.; Kim, J.; Ahn, C. -Y.; Jin, A.; Mun, J.; Sung, Y. -E. Bi-MOF Derived Micro/meso-porous Bi@C Nanoplates for High Performance Lithium-Ion Batteries. *Nanoscale*, **2020**, *12*, 15214

(4) Roy, P.; Srivastava, S. K. Nanostructured Anode Materials for Lithium Ion Batteries *J. Mater. Chem. A*, **2015**, *3*, 2454.

(5) Huggins, R. A. Advanced Batteries, Springer Science & Business Media, New York, USA, 2009.

(6) Xu, K. Nonaqueous Liquid Electrolytes for Lithium-Based Rechargeable Batteries *Chem. Rev.* **2004**, *104*, 4303.

[1.2]

(1) Berger, T.; Monllor-Satoca, D.; Jankulovska, M.; Lana-Villarreal, T.; Gomez, R. The Electrochemistry of Nanostructured Titanium Dioxide Electrodes. *ChemphysChem* **2012**, *13*, 2824.

(2) V. Koudriachova, M.; M. Harrison, N.; W. de Leeuw, S. Effect of Diffusion on Lithium Intercalation in Titanium Dioxide. *Phys. Rev. Lett.* **2001**, *86*, 1275.

(3) V. Koudriachova, M.; W. de Leeuw, S.; Orthorhombic Distortion on Li Intercalation in Anatase. *Phys. Rev. B.* **2004**, *69*, 054106.

- (4) Wagemaker, M.; Krol, R. v. d.; Kentgens, P. M.; Well, A. A. v.; Mulder, F. M. Two Phase Morphology Limits Lithium Diffusion in TiO₂(Anatase): A ⁷Li MAS NMR Study. *J. Am. Chem. Soc.* **2001**, *123*, 11454.
- (5) Wagemaker, M.; Kentgens, A. P. M.; Mulder, F. M. Equilibrium Lithium Transport between Nanocrystalline Phases in Intercalated TiO₂ Anatase. *Nature* **2002**, *418*, 397.
- (6) Wagemaker, M.; Kearley, G. J.; Well, A. A. v.; Mutka, H.; Mulder, F. M. Multiple Li Positions inside Oxygen Octahedra in Lithiated TiO₂ Anatase. *J. Am. Chem. Soc.* **2003**, *125*, 840.
- (7) Wagemaker, M.; Hecht, D. L.; Keil, P.; Well, A. A. v.; Frahm, R. Quasi-in-situ Reflection Mode Xanes at the Ti K-edge of Lithium Intercalated TiO₂ Rutile and Anatase. *Physica B*, **2003**, *336*, 118.
- (8) Wagemaker, M.; Borghois, W. J. H.; Mulder, F. M. Large Impact of Particle Size on Insertion Reactions. A Case for Anatase Li_xTiO₂. *J. Am. Chem. Soc.* **2007**, *129*, 4323.
- (9) Jiang, Y.; Liu, J. Definitions of Pseudocapacitive Materials: a Brief Review. *Energy Environ. Mater.* **2019**, *2*, 30.
- (10) Wang, J.; Polleux, J.; Lim, J.; Dunn, B. Pseudocapacitive Contributions to Electrochemical Energy Storage in TiO₂ (anatase) Nanoparticles. *J. Phys. Chem. C* **2007**, *111*, 14925.
- (11) Ganapathy, S.; Eck, E. R. H. v.; Kentgens, A. P. M.; Mulder, F. M.; Wagemaker, M. Equilibrium Lithium-Ion Transport between Nanocrystalline Lithium-Inserted Anatase TiO₂ and the Electrolyte. *Chem. Eur. J.* **2011**, *17*, 14811.
- (12) Belak, A. A.; Wang, Y.; Ven, A. V. d. Kinetics of Anatase Electrode: the Role of Ordering, Anisotropy, and Shape Memory Effects. *Chem. Mater.* **2012**, *24*, 2894.
- (13) Gentili, V.; Brutti, S.; Hardwick, L. J.; Armstrong, A. R.; Panero, S.; Bruce, P.

G. Lithium Insertion into Anatase Nanotubes. *Chem. Mater.* **2012**, *24*, 4468.

(14) Wagemaker, M.; Borghols, W. J. H.; Eck, E. R. H. v.; Kentgens, A. P. M.; Kearley, G. J.; Mulder, F. M. The Influence of Size on Phase Morphology and Li-Ion Mobility in Nanosized Lithiated Anatase TiO₂ *Chem. Eur. J.* **2007**, *13*, 2023.

[1.3]

(1) Lan, J. -L.; Jin, Y.; Qin, C.; Yu, Y.; Yang, X. Bio-Inspired Rose-Like Bi@Nitrogen-Enriched Carbon towards High-Performance Lithium-Ion Batteries. *ChemistrySelect* **2017**, *2*, 7178.

(2) Chai, W.; Yin, W.; Wang, K.; Ye, W.; Tang, B.; Rui, Y. Carbon-Coated Bismuth Nanospheres Derived from Bi-BTC as a Promising Anode Material for Lithium Storage. *Electrochim. Acta*, **2019**, *325*, 134927.

(3) Zhang, Y.; Wang, Q.; Wang, B.; Mei, Y.; Lian, P. N-doped Graphene/Bi Nanocomposite with Excellent Electrochemical Properties for Lithium-Ion Batteries. *Ionics*, **2017**, *23*, 1407.

(4) Yuan, H.; Jin, Y.; Chen, X.; Lan, J.; Yu, Y.; Yang, X. Large-Scale Fabrication of Egg-Carton-Inspired Bi/C Composite toward High Volumetric Capacity and Long-Life Lithium Ion Batteries. *ACS Sustainable Chem. Eng.* **2019**, *7*, 6033.

(5) Hong, W.; Ge, P.; Jiang, Y.; Yang, L.; Tian, Y.; Zou, G.; Cao, X.; Hou, H.; Ji, X. Yolk-Shell-Structured Bismuth@N-Doped Carbon Anode for Lithium-Ion Battery with High Volumetric Capacity. *ACS Appl. Mater. Interfaces*, **2019**, *11*, 10829.

(6) Zhou, J.; Chen, J.; Chen, M.; Wang, J.; Liu, X.; Wei, B.; Wang, Z.; Li, J.; Gu, L.; Zhang, Q.; Wang, H.; Guo, L. Few-Layer Bismuthene with Anisotropic Expansion for High-Areal-Capacity Sodium-Ion Batteries. *Adv. Mater.* **2019**, *31*, 1807874.

(7) Finke, A.; Poizot, P.; Guery, C.; Dupont, L.; Taberna, P. -L. Simon, P.; Tarascon, J. -M. Electrochemical Method for Direct Deposition of Nanometric Bismuth and Its

- Electrochemical Properties vs Li *Electrochem. Solid-State Lett.* **2008**, *11*, E5.
- (8) Liu, S.; Feng, J.; Bian, X.; Liu, J.; Xu, H. Advanced Arrayed Bismuth Nanorod Bundle Anode for Sodium-Ion Batteries. *J. Mater. Chem. A*, **2016**, *4*, 10098.
- (9) Hong, W.; Wang, A.; Li, L.; Qiu, T.; Li, J.; Jiang, Y.; Zou, G.; Peng, H.; Hou, H.; Ji, X. Bi Dots Confined by Functional Carbon as High-Performance Anode for Lithium Ion Batteries. *Adv. Funct. Mater.* **2021**, *31*, 2000756.
- (10) Xiong, P.; Bai, P.; Li, A.; Li, B.; Cheng, M.; Chen, Y.; Huang, S.; Jiang Q.; Bu, X. -H.; Xu, Y. Bismuth Nanoparticle@Carbon Composite Anodes for Ultralong Cycle Life and High-Rate Sodium-Ion Batteries. *Adv. Mater.* **2019**, *31*, 1904771.
- (11) Wang, L.; Voskanyan, A. A.; Chan, K. Y.; Qin, B.; Li, F. Combustion Synthesized Porous Bismuth/N-Doped Carbon Nanocomposite for Reversible Sodiation in a Sodium-Ion Battery. *ACS Appl. Energy Mater.* **2020**, *3*, 565.
- (12) Voskanyan, A. A.; Ho, C. -K.; Chan, K. Y. 3D δ -MnO₂ Nanostructure with ultralarge Mesopores as High-Performance Lithium-Ion Battery Anode Fabricated via Colloidal Solution Combustion. *J. Power Sources*, **2019**, *421*, 162.
- (13) Varma, A.; Mukasyan, A. S.; Rogachev, A. S.; Manukyan, K. V. Solution Combustion Synthesis of Nanoscale Materials. *Chem. Rev.* **2016**, *116*, 14493.
- (14) Han, Y.; Qi, P.; Feng, X.; Li, S.; Fu, X.; Li, H.; Chen, Y.; Zhou, J.; Li, X.; Wang, B. In Situ Growth of MOFs on the Surface of Si Nanoparticles for Highly Efficient Lithium Storage: Si@MOF Nanosomposites as Anode Materials for Lithium-Ion Batteries. *ACS Appl. Mater. Interfaces*, **2015**, *7*, 2178.
- (15) Zhong, Y.; Li, B.; Li, S.; Xu, S.; Pan, Z.; Huang, Q.; Xing, L.; Wang, C.; Li, W. Bi Nanoparticles Anchored in N-Doped Porous Carbon as Anode of High Energy Density Lithium ion Battery *Nano-Micro Lett.* **2018**, *10*, 56.
- (16) H. Chen; M. Ling; L. Hencz; H. Y. Ling; G. Li; Z. Lin; G. Liu; S. Zhang Exploring chemical, mechanical, and electrical functionalities of binders for

advanced energy-storage devices *Chem. Rev.* **2018**, 118, 8936.

(17) Omori, Y.; Honma, T.; Komatsu, T. Formation of Bismuth Metal in bismuth Borate Glass by Reductive Heat Treatment and Its Electrochemical Property as Anode in Lithium Ion Battery. *J. Ceram. Soc. Jpn.* **2018**, 126, 820.

Chapter 2. Operando Identification of the Chemical and Structural Origin of Li-Ion battery Aging at Near-Ambient Temperature

Note: Studies on this part was written based on, and figures are based on the work conducted with Byoung-Hoon Lee and Jaehyuk park (co-first author), published in *Jouarnal of the American Chemical Society* **2020**, *142*, 13406.

2.1. Introduction

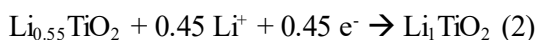
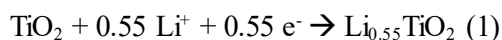
Development of the lithium-ion battery (LIB) has revolutionized energy storage systems.¹⁻⁴ Since LIBs and energy-consuming components are integrated as a compact device, generated heat can easily increase the working temperature, and LIBs in modern applications often operate at 20–40 °C higher than the ambient temperature. Importantly, investigation of macroscopic LIB performance in such mild thermal environment indicates significant reduction of battery lifespan and accelerated battery aging.⁵⁻⁹ However, operando identification of fundamental reason behind the battery aging is very difficult because complex battery components (electrolyte, cathode & anode materials, and separator) and working processes are interrelated.⁶⁻⁹

Understanding the origin of battery aging in mild thermal environment is especially crucial in industrially important intercalation-based materials because recent spectroscopic advances have shown lithium storage in intercalation-based materials can undergo various abnormal storage mechanisms that significantly affect battery performance.¹⁰⁻²¹ These include anionic redox,¹¹ double redox,¹² single phase,^{13,14} and sequential phase transition,^{10,20} which have recently attracted extensive research interest for the design of high-performance electrode materials. Various factors such

as applied voltage, material composition, and particle size have been reported to initiate abnormal storage mechanism by controlling kinetics and thermodynamics of lithium intercalation.

Temperature is an important factor that can cause substantial change in lithium intercalation chemistry. Various commercial intercalation-based materials including, graphite, LiCoO₂, LiMn₂O₄, and Li(Ni,Mn,Co)O₂ have experienced severe capacity loss at higher temperature.⁷⁻⁹ Intra-granular crystal cracking and irreversible intercalation of lithium ions in the crystal lattice were often identified as undesired abnormal lithium storage mechanisms that rapidly deactivate LIBs as a consequence.^{8,22,23} Therefore, operando identification of microscopic chemical and structural origin of this drastic decay of LIB performance in mild thermal condition is crucial for the design of high-performance LIB for modern applications that operate at high temperatures.

Anatase TiO₂ has been extensively investigated in various energy applications due to their abundance, environmental benignity and material stability.^{10,20,24-38} As a potential substitute of graphite, various strategies including design of nanostructures with various morphologies,^{20,30,33,34,38} controlling crystal size,^{10,20,35} and formation of multicomponent heterostructure^{27,31,32} have proven to be effective on enhancing Li-ion storage with high-rate capability and long-term cyclic stability. On the other hand, as an intercalation compound, it has been recently reported to undergo abnormal lithium storage that depends on various factors.^{10,15,20,24,25}



Lithium intercalation on anatase TiO₂ is known to involve phase transition of tetragonal anatase TiO₂ to orthorhombic Li_{0.55}TiO₂ (equation 1).²⁴ Downsizing crystal size below 7 nm enables to intercalate excess-lithium through second phase transition by forming tetragonal Li₁TiO₂ (equation 2). Although this abnormal

lithium intercalation was identified to induce irreversible capacity loss upon cycling,¹⁰ it has later been shown that this second phase transition can be reversibly maintained for long-term usage when small-sized crystals (~7 nm) are interconnected in nanostructure.²⁰ Therefore, anatase TiO₂ nanostructure can be a model intercalation compound that possesses controllable abnormal lithium intercalation characteristics to investigate operando identification of fundamental reason behind the battery aging in mild thermal environment.

Herein, we focus on identifying operando chemical and structural origin of battery aging that occurs at near-ambient temperatures using anatase TiO₂ as a model intercalation compound. By combining electrochemical measurements, atomic-level electron microscopy, and in situ analyses we show mild thermal condition, as low as 45°C, can initiate abnormal lithium intercalation. Although this abnormal lithium intercalation enables excess lithium storage in the first few cycles, it cracks the crystals due to severe intra-crystal stress, which deactivates the electrode materials and consequently prevents long-term usage. It is notable that the deformation of the crystal structure induced by mild thermal environment causes irreversible capacity loss. Our work provides important insight on how mild thermal environment initiates and accelerates battery aging in intercalation-based electrode materials.

2.2. Experimental

Materials. Titanium (IV) n-butoxide (TBOT) was purchased from Strem Chemicals, Inc. (Newburyport, MA 01950-4098, USA). Tetraethyl orthosilicate (TEOS), resorcinol, formaldehyde solution (37 wt% in H₂O) and polyvinylpyrrolidone (PVP) (MW = 55,000) were purchased from Sigma Aldrich (St. Louis, MO, USA). Acetonitrile (98 %), anhydrous ethanol (99.9%), sodium hydroxide (NaOH) and aqueous ammonia solution (28 – 30 wt%) were purchased from Samchun Chemical (Seoul, Korea). All reagents were used as received without further purification.

Synthesis of 12 NT. Synthesis of 12 NT were based on layer-by-layer sol-gel coating method modified from previous reports (See ref. 27 and 35 in main text for details). Briefly, SiO₂ NP was synthesized using Stöber method. TEOS (99%, 0.86 ml) was added in a mixture solution of EtOH (23 ml), H₂O (4.3 ml) and aqueous ammonia (28-30 wt%, 0.6ml). After vigorously stirring for 6 h, reaction product (SiO₂ NP) was washed with water and ethanol. For TiO₂ overlayer coating, the prepared SiO₂ NP was dispersed in 40 ml of anhydrous ethanol. Then aqueous ammonia (28 – 30 wt%, 0.4 ml) and acetonitrile (98%, 14 ml) were added on the SiO₂ NP solution. The resulting solution was sonicated for 10 min to obtain well-dispersed SiO₂ NP prior to TiO₂ overlayer coating. Meanwhile, TBOT (0.8 ml) was added in the mixture of anhydrous ethanol (99.9%, 6 ml) and acetonitrile (98%, 2 ml) (solution 2). Solution 2 was added to SiO₂ NP solution and vigorously stirred for 3 h for TiO₂ overlayer coating. Resulting SiO₂@TiO₂ NP solution was washed with ethanol and water. For resorcinol-formaldehyde overlayer coating, the above SiO₂@TiO₂ NP was dispersed in H₂O (56 ml). Aqueous CTAB solution (2 mL, 0.01 M) was added on the above solution. After vigorous stirring for 1 h, resorcinol (0.08 g), formaldehyde (37 wt%, 0.112 ml) and diluted aqueous ammonia solution (2.8-3.0 wt%, 0.4 ml) were added. After 24 h of reaction, the resulting SiO₂@TiO₂@RF NP was washed with ethanol and water. The products were dried in convection oven at 80°C overnight. For

crystallization of amorphous TiO₂ and calcination of RF layer, SiO₂@TiO₂@RF NP was heated at 750 °C (static air, 150 °C h⁻¹ and 2 h). Note that initial brown powder becomes white after calcination due to RF overlayer calcination. For SiO₂ etching, calcined SiO₂@TiO₂@RF NP was dispersed in NaOH solution (0.5 M) and heated to 90 °C under continuous stirring. After stirring for 6 h, the product was washed with H₂O and ethanol, and dried overnight in a convection oven at 80 °C. The resulting 12 NT was used for various electrochemical measurements and characterizations without further modification.

Electrochemical measurement. The slurry of working electrodes is prepared by mixing active materials (12 NT), Super P and poly(vinylidene fluoride) (PVDF) in N-Methyl-2-pyrrolidone (NMP) (Sigma-Aldrich) with a weight ratio of 8:1:1. The evenly blended slurry is casted on the Cu current collector by doctor blade method and dried in vacuum at 120 °C for 8 h. The electrochemical cells (CR2032 type coin cell) were assembled in the Ar-filled glove box. Lithium metal was used as reference electrodes. Poly (ethylene) was used as separator and 1M LiPF₆ in ethylene carbonate (EC)/diethyl carbonate (DEC) (1:1 v/v) as electrolyte. Electrochemical tests were performed using WBCS3000 (WonAtech, Korea) in a voltage range of 1.0-2.5 V at four different temperatures (RT, 45 °C, 60 °C, and 90 °C).

Characterization. Transmission electron microscopy (TEM) was performed on a JEOL EM-2010 microscope at 200 kV operation. The field emission scanning electron microscopy (FESEM) was performed on a JEOL JSM-7800F-Prime microscope. Cs-corrected scanning transmission microscopy (Cs-STEM) imaging was performed using a spherical aberration-corrected JEM ARM-200F microscope (Cold FEG Type, JEOL), installed at the National Center for Inter-University Research Facilities (NCIRF) at Seoul National University. X-ray diffraction analysis was conducted on a Rigaku D/MAX-2500H system employing Cu K α radiation. Collected data were analyzed by pattern fitting using HighScore Plus software.

Characterization of *operando* heating XRD experiments. To apply transmission

operando heating XRD analysis, a customized coin cell with a hole in the center and Cu mesh electrode was used to reduce interference of Cu substrate. *Operando* XRD patterns were collected using Smartlab (Rigaku, Japan) with Cu K α radiation (1.5406 Å). Each cell was discharged and charged at a current density of 25 mA g⁻¹ in same voltage range at RT and 60 °C. An XRD pattern was obtained at intervals of about 28 min. The obtained spectra were processed using PDXL software.

2.3. Results and discussion

Material selection is very important to investigate chemical and structural origin of battery aging on mild thermal condition, since materials of focus should possess well-known lithium intercalation mechanism with prolonged cyclic stability in the ordinary working temperature. Here, we choose anatase TiO₂ nanostructure composed of 12 nm-sized individual crystals (12 NT), because lithium intercalation in anatase TiO₂ nanocrystals is well understood as a single-phase transition process (equation 1) and designed nanostructures have shown to successfully stabilize long-term lithium intercalation.^{10,20,24-26} 12 NT was prepared using sacrificial template method with modifications from the previous reports (Figure 2.3.1 and 2.3.2).^{28,39} Transmission electron microscopy (TEM) image, field emission scanning electron microscopy (FESEM) and X-ray diffraction (XRD) pattern of 12 NT shows well-developed hollow structure that is composed of interconnected 12 nm-sized individual anatase TiO₂ nanocrystals (Figure 2.3.3-2.3.6). To investigate the impact of thermal environment on battery performance, galvanostatic lithiation/delithiation was performed on 12 NT at four different temperatures (RT, 45 °C, 60 °C and 90 °C) (Figure 2.3.7 and Figure 2.3.8, 2.3.9). The electrochemical measurements show the characteristics of typical anatase TiO₂ at RT, with kinetic capacity of 180 mAh g⁻¹ and a cathodic peak around 1.75 V in cyclic voltammetry (CV), corresponding to the first plateau through typical intercalation reaction (TiO₂ \rightarrow Li_{0.55}TiO₂). Higher capacity was observed at higher temperatures. Notably, capacities from the first plateau are similar at various temperatures, with the extra capacity attributed to the

extension in the low-voltage slope region. The extension of this region became more prominent at higher temperatures. Lithium intercalation in the low-voltage slope region has two possibilities: interfacial pseudo-capacitive charge storage,^{32,33,40,41} and excessive lithium intercalation through sequential phase transition from $\text{Li}_{0.55}\text{TiO}_2$ to Li_1TiO_2 .^{10,20} In contrast to the voltage profile at RT, a distinct pseudo-plateau appeared in the voltage profile at higher temperatures (indicated by dotted box, Figure 2.3.7.B). These findings were further supported by CV analysis, in which second cathodic peak (~ 1.5 V) started to appear as low as 45 °C, and became prominent as the operating temperature increases, suggesting thermal environment can greatly affect lithium intercalation mechanism even at near-ambient temperature.

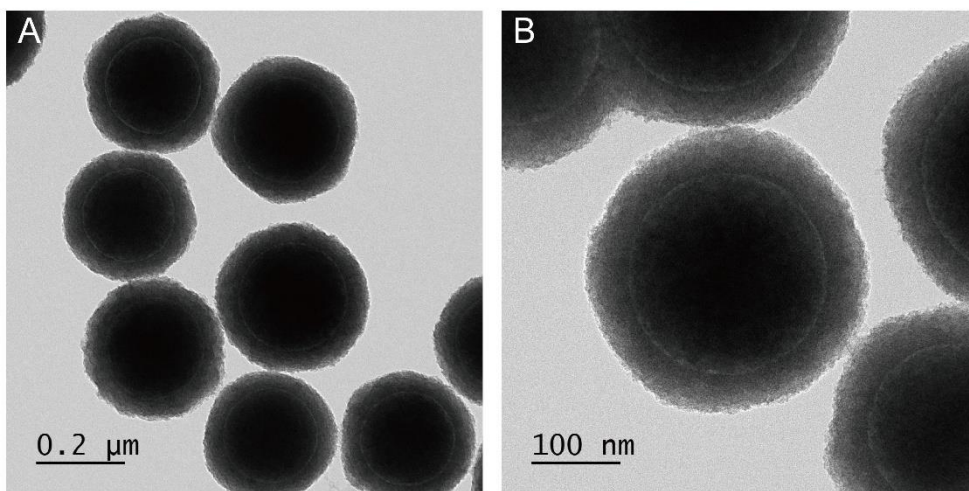


Figure 2.3.1. Representative TEM images of $\text{SiO}_2@\text{TiO}_2@\text{RF}$.

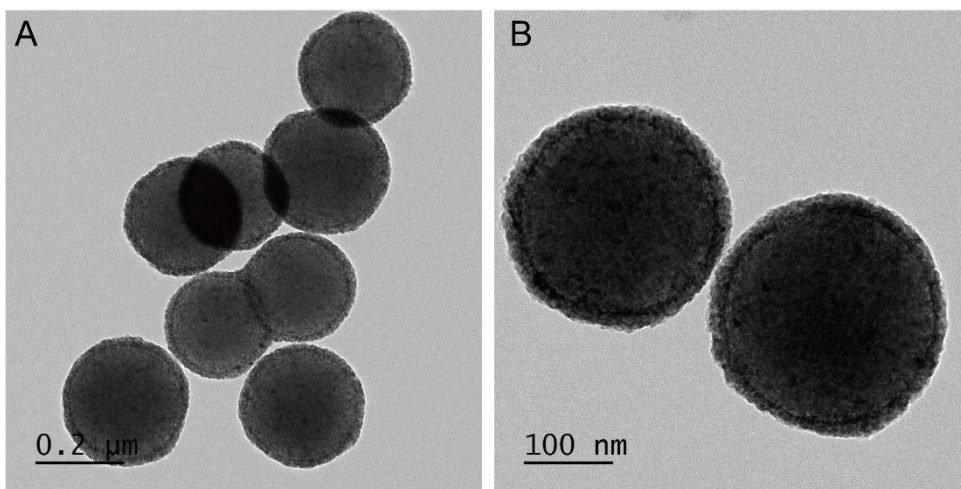


Figure 2.3.2. Representative TEM images of $\text{SiO}_2@\text{TiO}_2@\text{RF}$ after calcination (750 °C, static air). RF polymers are removed after high temperature calcination. Amorphous TiO_2 layer crystallize into outer-shell comprising numerous 12 nm-sized anatase TiO_2 nanocrystals.

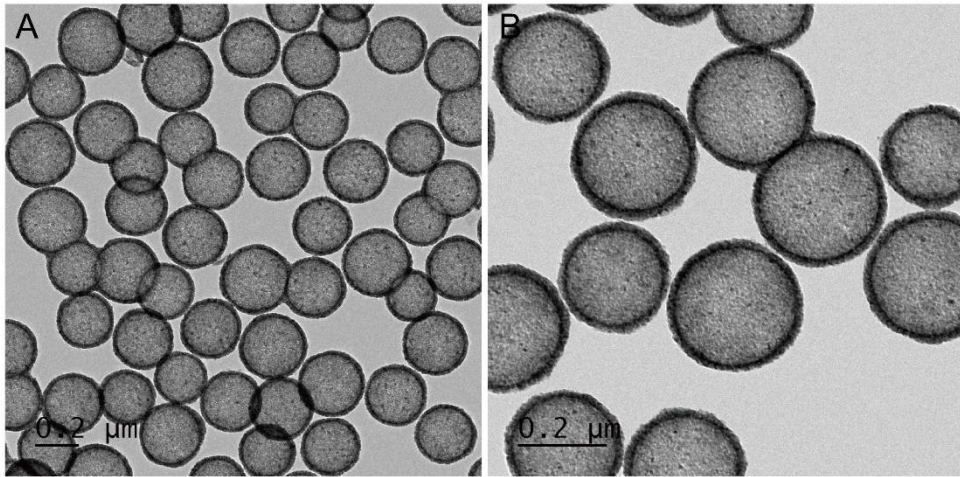


Figure 2.3.3. Low magnification TEM image of synthesized 12 NT after etching SiO₂ core.

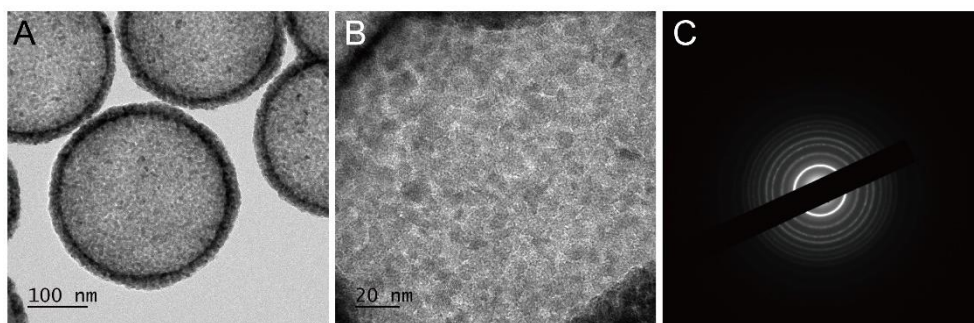


Figure 2.3.4. High magnification TEM image (A, B) and selected area diffraction pattern (C) of synthesized 12 NT.

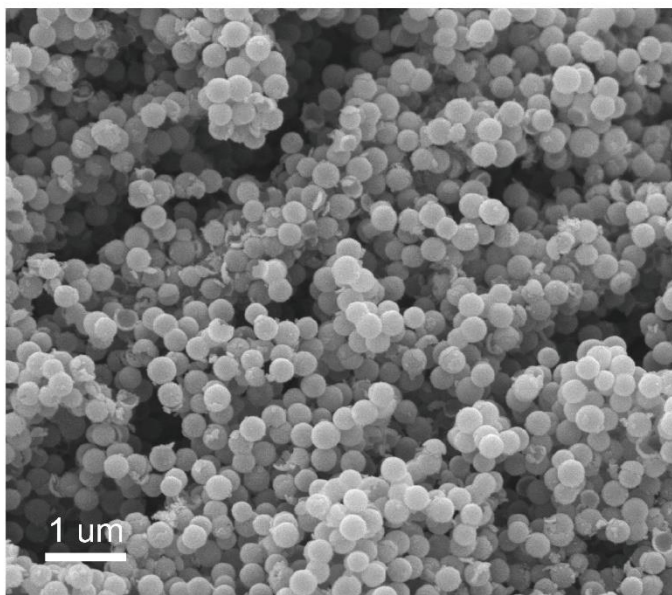


Figure 2.3.5. Representative FESEM image of 12NT

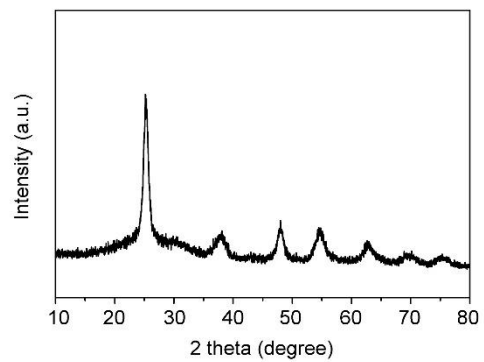


Figure 2.3.6. XRD pattern of as-prepared 12 NT

(Figure 2.3.7.C, D and Figure 2.3.8, 2.3.9). From the galvanostatic measurements in different thermal conditions, we can conclude that an anomalous lithium storage occurs, which significantly affects the battery performance at a temperature as low as 45 °C. To elucidate the structural and chemical impact of thermal environment on lithium intercalation mechanism, *operando* XRD analysis was performed (Figure 2.3.10, see Figure 2.3.11 for *operando* heating XRD measurement setup). From the first lithiation cycle, we found that 12 NT reacts with more lithium at 60 °C (0.75 Li) than RT (0.55 Li) (Figure 2.3.10.A). Figure 2.3.10.B and 2.3.10.C show *operando* XRD patterns during the first cycle of discharge/charge process at RT and 60 °C, respectively. At RT, phase transition to $\text{Li}_{0.55}\text{TiO}_2$ starts by reacting with 0.27 lithium (point b). The orthorhombic $\text{Li}_{0.55}\text{TiO}_2$ structure maintains until the reaction finishes with 0.55 lithium (point c). The reversible emergence of (011) plane peaks and a slight peak shift of (101) and (200) plane shows typical phase transition ($\text{TiO}_2 \rightarrow \text{Li}_{0.55}\text{TiO}_2$) during lithiation/delithiation cycle. At 60 °C, $\text{Li}_{0.55}\text{TiO}_2$ appears by reacting with 0.32 lithium (point g) and maintains the crystal structure until reacting with 0.55 lithium (point h), which is confirmed by the appearance of (011) peak and a slight peak shift of (101). Interestingly, at 60 °C, orthorhombic $\text{Li}_{0.55}\text{TiO}_2$ phase maintains only until reacting with 0.55 Li, and an additional phase transition to tetragonal Li_1TiO_2 is observed by intercalating additional lithium (~ 0.75 Li, point i). After the complete lithium intercalation, characteristic peaks corresponding to $\text{Li}_{0.55}\text{TiO}_2$ disappears and a new single peak around 24.5° appears, which can be assigned to (101) plane of tetragonal Li_1TiO_2 phase (24.3°). Disappearance of (200) plane peak around 48° is simultaneously observed, which is consistent with the transformation of $\text{Li}_{0.55}\text{TiO}_2$ to Li_1TiO_2 (point i). This sequential phase transition ($\text{TiO}_2 \rightarrow \text{Li}_{0.55}\text{TiO}_2 \rightarrow \text{Li}_1\text{TiO}_2$) is also reversible during delithiation (point i to l), indicating the higher capacity at higher temperatures is from the excess-lithium intercalation in Li_1TiO_2 . Since anatase TiO_2 and Li_1TiO_2 have the identical tetragonal crystal structure, lithium ion insertion causes an expansion along the a and b axis in the crystal structure (Figure 2.3.12), which is supported by the peak shift of (101)

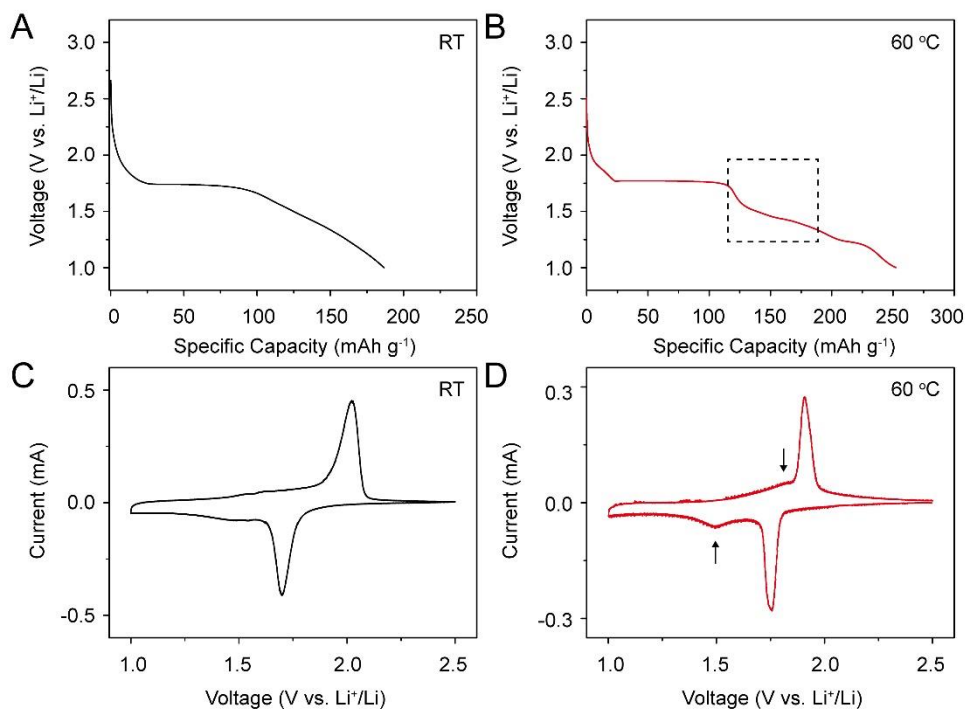


Figure 2.3.7. Electrochemical properties of anatase TiO_2 anodes. Voltage profiles of 12 NT during the initial discharge at a current density of 100 mA g^{-1} at A) RT and B) $60 \text{ }^\circ\text{C}$. Cyclic voltammograms of 12 NT at a scan rate of 0.1 mV s^{-1} at C) RT and D) $60 \text{ }^\circ\text{C}$.

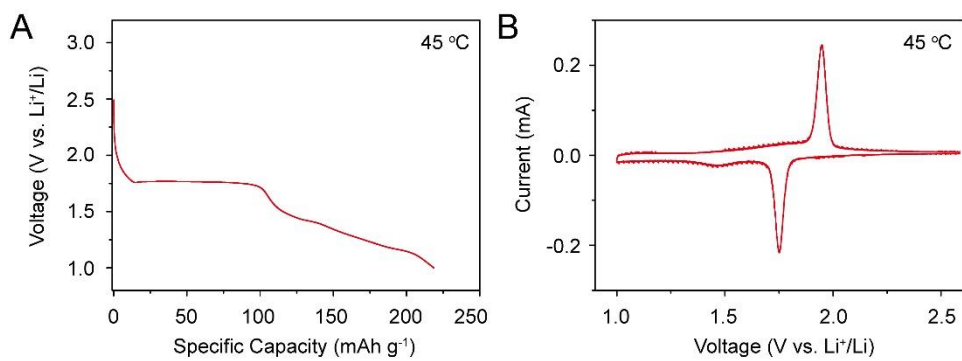


Figure 2.3.8. (A) Voltage profile (current density of 100 mA g⁻¹) and (B) cyclic voltammetry (scan rate of 0.1 mV s⁻¹) of 12 NT at 45 °C.

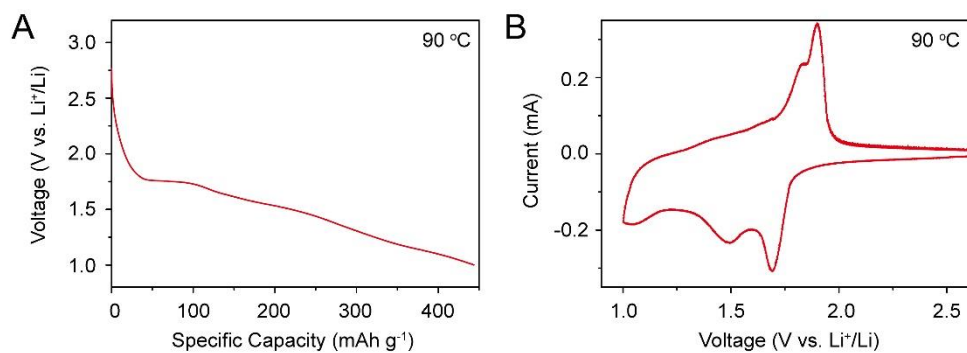


Figure 2.3.9. (A) Voltage profile (current density of 100 mA g⁻¹) and (B) cyclic voltammetry (scan rate of 0.1 mV s⁻¹) of 12 NT at 90 °C.

plane to a lower angle. Then, we extracted d -value of the (101) plane (anatase TiO_2 and Li_1TiO_2) and the (011) plane ($\text{Li}_{0.55}\text{TiO}_2$) from *in situ* XRD patterns to investigate the impact of mild thermal condition on lattice parameters during lithiation cycle (Figure 2.3.13). Initially, d -value of (101) planes remain constant as the transformation to $\text{Li}_{0.55}\text{TiO}_2$ occurs. Subsequently, (011) peak appears, which also remains constant (JCPDS CardNo. 38-0269). At 60 °C, as additional phase transition from $\text{Li}_{0.55}\text{TiO}_2$ to Li_1TiO_2 progresses, (011) peak disappears and d -value of (101) peak rapidly increases and reaches 3.61 Å at 0.75 Li. Although this value is somewhat smaller than that of Li_1TiO_2 (101) plane (3.67 Å), the trend of increasing d -value for (101) plane appears only at 60 °C, demonstrating the mild thermal condition can expand lattice parameters through directing an additional phase transition. Through comprehensive analysis on *in situ* XRD patterns and d -values, we conclude that mild thermal condition accelerates lithium intercalation kinetics and induces anomalous phase transition that leads to excess-lithium storage in Li_1TiO_2 phase which does not take place at RT (Figure 2.3.10D). From this point, it is apparent that thermal environment can perturb and eventually change the lithium intercalation chemistry even at near-ambient temperature. Because macroscopic investigations on thermal environment have been reported to accelerate battery aging in various materials,⁵⁻⁹ we then focused on how the perturbed lithium intercalation chemistry in mild thermal environment can accelerate battery aging. First, the voltage profiles are divided into two regions (Figure 2.3.14). Region 1 includes the voltage plateau where general Li intercalation from anatase TiO_2 to $\text{Li}_{0.55}\text{TiO}_2$ occurs. Region 2 includes low-voltage slope, where additional transformation to Li_1TiO_2 takes place under mild thermal condition. We monitored the ratio of Region 1 and 2 for long-term cycling at various temperatures. Figure 3B summarizes the voltage profile and ratio of region 1 to region 2, operated at 60 °C in the 2nd, 20th, 40th cycles. Region 1 composes 45.9% of the total capacity in the 2nd cycle, which rapidly decreases upon cycling, reaching only 5.5% in the 40th cycle. This phenomenon is further evidenced by significant shortage of the flat plateau in the voltage profile

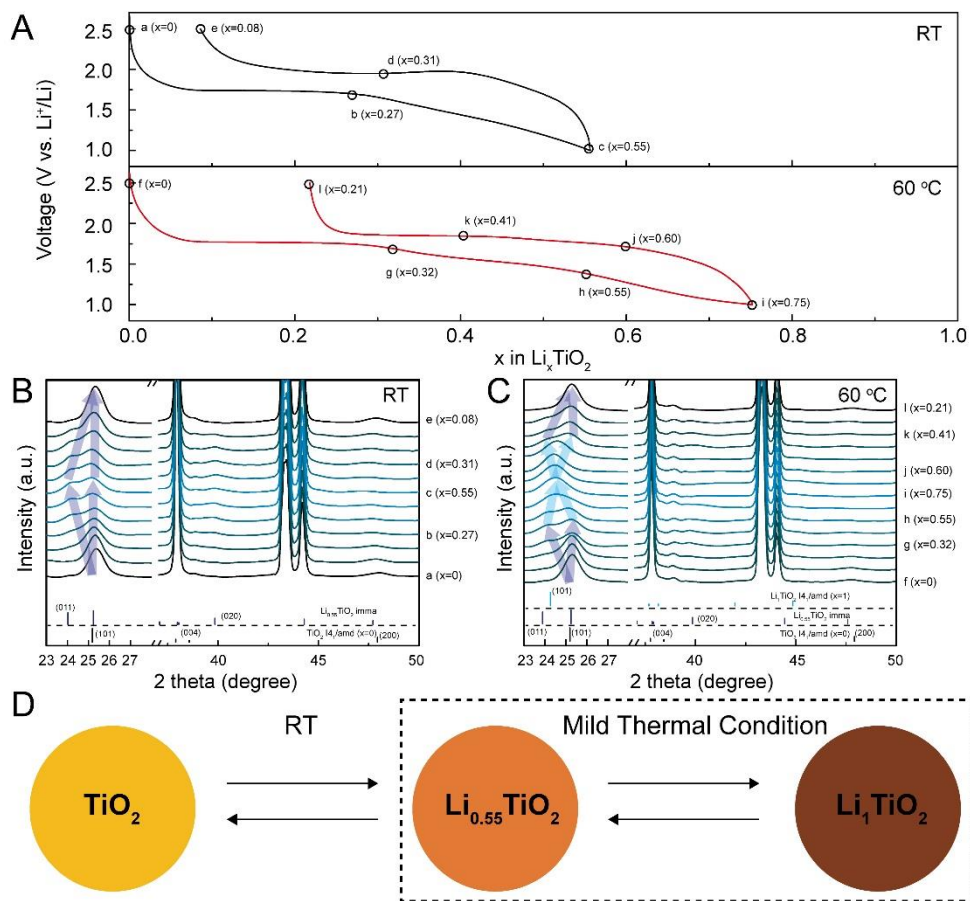


Figure 2.3.10. *In situ* XRD analysis during the first cycle. A) Voltage profiles of 12 NT in the first cycle at RT (up) and 60 °C (down). Series of *in situ* XRD patterns for charge-discharge of 12 NT at B) RT and C) 60 °C in the first cycle. D) Schematic of crystal structure transformation of lithium intercalation on anatase TiO₂ in RT and mild thermal condition (dotted box).

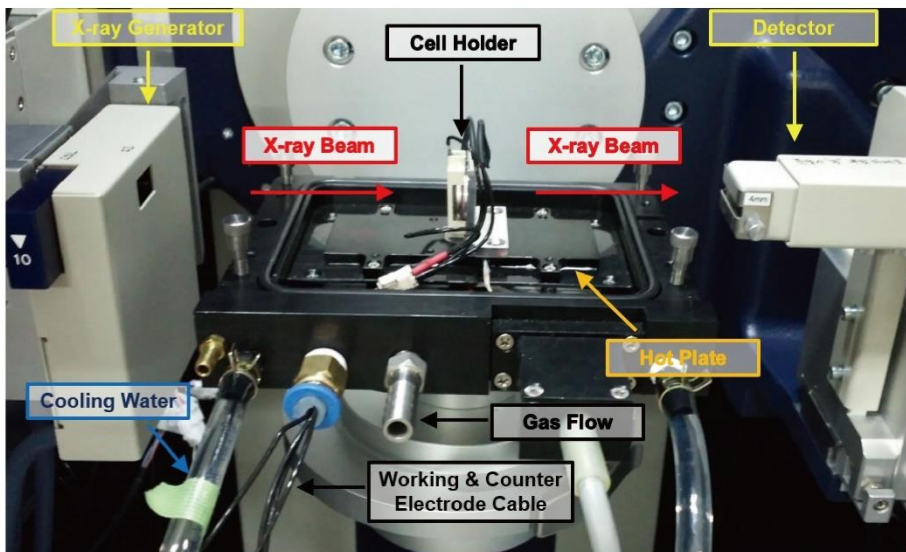


Figure 2.3.11. Custom-made *operando* heating XRD measurement setup.

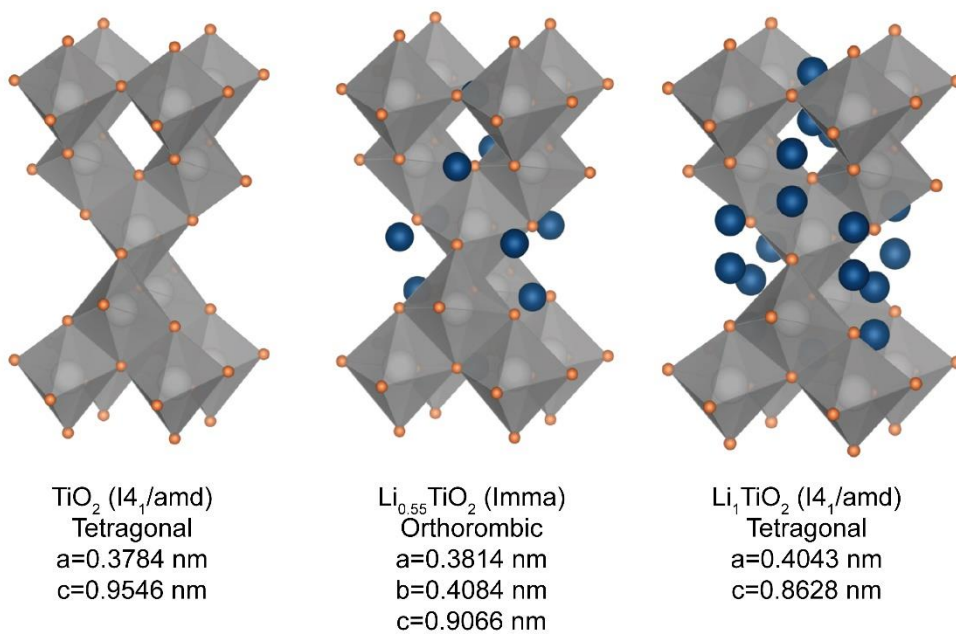


Figure 2.3.12. Crystal structure of anatase TiO_2 during phase transition: (A) anatase TiO_2 , (B) $\text{Li}_{0.55}\text{TiO}_2$ and (C) Li_1TiO_2 .

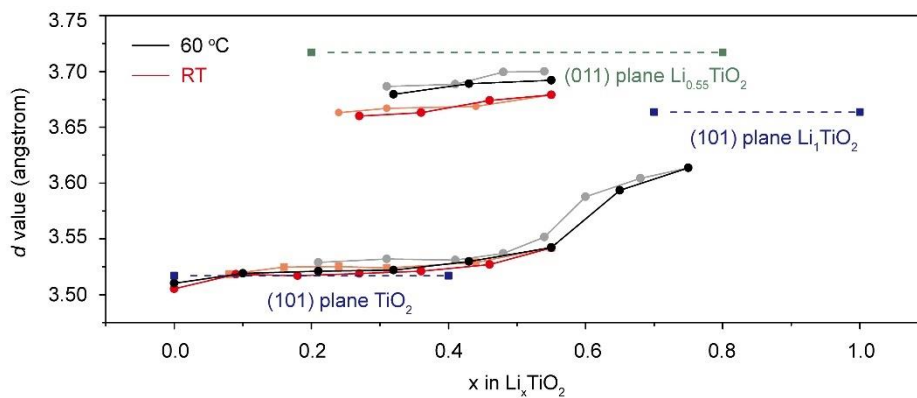


Figure 2.3.13. d values of the (101) planes (TiO_2 and Li_1TiO_2) and the (011) plane ($\text{Li}_{0.55}\text{TiO}_2$) extracted from Figure 2.3.10.B and C (*in situ* XRD results).

(guided by arrow, Figure 2.3.14.A). At RT, this phenomenon was not observed and the capacity of Region 1 was stable upon cycling with a minimal decrease ($2^{\text{nd}} \rightarrow 52.0 \text{ mAh g}^{-1}$, $20^{\text{th}} \rightarrow 40.0 \text{ mAh g}^{-1}$, $40^{\text{th}} \rightarrow 34.9 \text{ mAh g}^{-1}$) (Figure 2.3.15). Furthermore, the drastic decrease on Region 1 accelerates at a higher temperature (at $90 \text{ }^{\circ}\text{C}$, $2^{\text{nd}} \rightarrow 25.5 \text{ mAh g}^{-1}$, $20^{\text{th}} \rightarrow 1.9 \text{ mAh g}^{-1}$, $40^{\text{th}} \rightarrow 1.8 \text{ mAh g}^{-1}$) (Figure 2.3.16). Therefore, mild thermal environment is shown to induce excess lithium storage in the first few cycles through additional phase transition but rapidly deteriorates battery performance in the subsequent cycling. Since Region 1 represents the general transformation of anatase TiO_2 to $\text{Li}_{0.55}\text{TiO}_2$, the performance deterioration in mild thermal environment originates from the hindered intercalation in anatase TiO_2 . Based on our finding that the mild thermal condition can induce the reversible formation of Li_1TiO_2 phase, we hypothesize that the unexpected Li_1TiO_2 formation limits the lithium intercalation in anatase TiO_2 upon cycling in mild thermal environment.

To clarify this issue, *in situ* XRD was performed in the 10^{th} and 20^{th} cycles at $60 \text{ }^{\circ}\text{C}$ (Figure 2.3.17). It should be noted that in the 10^{th} cycle, a distinct shoulder peak is present below the (101) peak of anatase TiO_2 , suggesting that not only anatase TiO_2 but also $\text{Li}_{0.55}\text{TiO}_2$ and Li_1TiO_2 co-exist, even before the battery-cell operation (guided by arrow, Figure 2.3.17.B). This result reveals that some lithium ions are trapped in the crystal lattice and cannot be completely delithiated. However, sequential phase transition ($\text{TiO}_2 \rightarrow \text{Li}_{0.55}\text{TiO}_2 \rightarrow \text{Li}_1\text{TiO}_2$) is reversibly observed to a certain extent during the discharging/charging process in the 10^{th} cycle, demonstrating the prolonged impact of mild thermal environment. In the 20^{th} cycle, the distinct shoulder peak around 24° becomes more prominent, suggesting that incomplete delithiation accumulates and gradually blocks the lithium intercalation path in anatase TiO_2 (guided by arrow, Figure 2.3.17.C). Such irreversible lithium ion trapping was also observed in industrial LiCoO_2 cathode aged at high temperature, and therefore it is very important to understand how it affects battery aging.^{5,8}

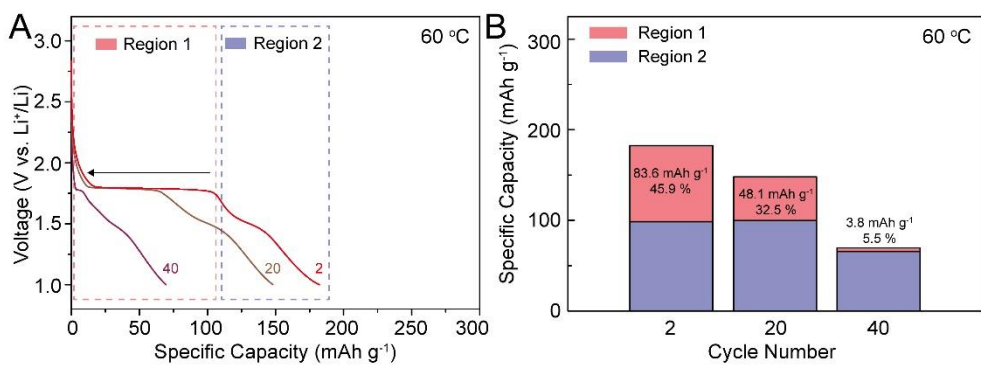


Figure 2.3.14. A) Voltage profiles of 12 NT at a current density of 100 mA g⁻¹ in the 2nd, 20th, 40th cycles at 60 °C. B) Capacity and ratio of region 1 and 2 in 12 NT in the 2nd, 20th, 40th cycles at 60 °C.

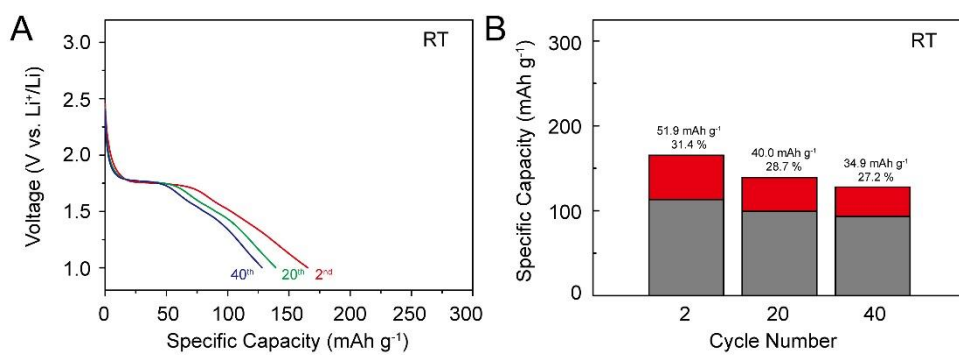


Figure 2.3.15. A) Voltage profiles of anatase TiO₂ at a current density of 100 mA g⁻¹ in the 2nd, 20th, 40th cycles at RT. B) Capacity and ratio of region 1 and 2 in anatase TiO₂ in the 2nd, 20th, 40th cycles at RT.

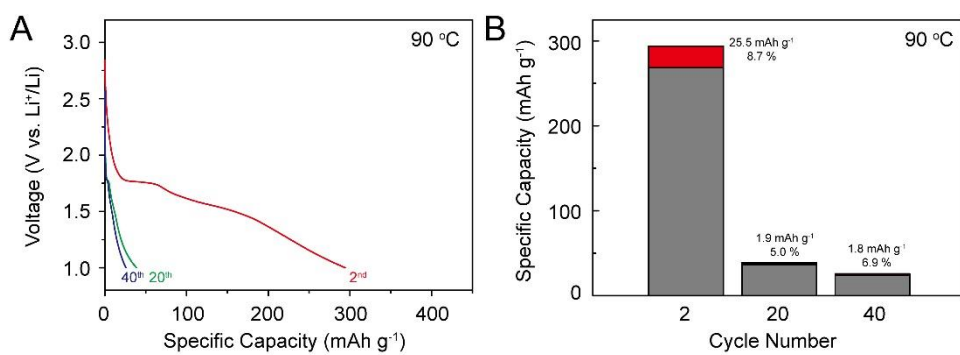


Figure 2.3.16. A) Voltage profiles of anatase TiO₂ at a current density of 100 mA g⁻¹ in the 2nd, 20th, 40th cycles at 90 °C. B) Capacity and ratio of region 1 and 2 in anatase TiO₂ in the 2nd, 20th, 40th cycles at 90 °C.

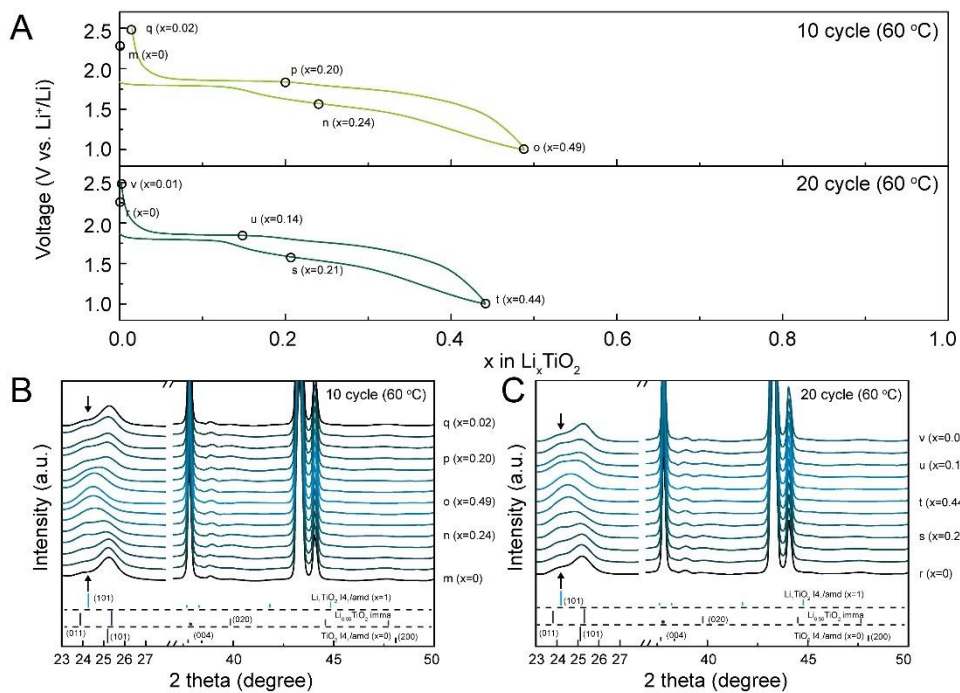


Figure 2.3.17. *In situ* XRD analysis at prolonged cycles. A) Voltage profiles of 12 NT at 60 °C in 10th cycle (up) and 20th cycle (down). Series of *in situ* XRD patterns for charge-discharge of 12 NT at 60 °C in B) 10th cycle and C) 20th cycle.

Figure 2.3.18 presents Cs-corrected scanning transmission electron microscope (Cs-STEM) image performed on 12 NT after the 20th lithium intercalation cycle at 60 °C (point r in Figure 2.3.17.C). Low magnification STEM image reveals that the hollow nanostructure composed of the interconnected primary nanocrystals is well preserved during the cycling process (Figure 2.3.18.A and Figure 2.3.19). This result is in accordance with the previous reports that various nanostructures composed of interconnected constituent nanocrystals can enhance cyclic stability.^{20,30-34} Interestingly, however, Cs-high magnification bright field (BF)-STEM images (Figure 2.3.18.B, C and Figure 2.3.20) reveal that the constituent nanocrystals were fragmented to smaller nanocrystals with abrupt interfaces (guided by white dotted lines in Figure 2.3.18.C). In contrast, both the hollow nanostructure and primary nanocrystals are well preserved, where abrupt interfaces on the nanocrystals are not observed in the Cs-STEM images of 12 NT after the 20th lithium intercalation cycle at RT (Figure 2.3.21). Apparent XRD peak broadening was observed after the 20th lithium intercalation cycle at 60 °C, and the average crystal size calculated from the Scherrer equation confirmed the decrease of crystal size upon cycling (1st cycle, 11.5 nm and 20th cycle, 9.6 nm) (Figure 2.3.22). At RT, the crystal size change is negligible (1st cycle, 11.4 nm and 20th cycle, 11.1 nm). Considering that the 2nd phase transition does not occur at RT, negligible crystal size change at RT implies that the crystal cracking majorly occurs in the 2nd phase transition ($\text{Li}_{0.55}\text{TiO}_2 \rightarrow \text{Li}_1\text{TiO}_2$) (Figure 2.3.23).

Generally, sequential phase transition ($\text{TiO}_2 \rightarrow \text{Li}_{0.55}\text{TiO}_2 \rightarrow \text{Li}_1\text{TiO}_2$) is prohibited for anatase TiO_2 particles larger than 7 nm.¹⁰ However, we found that mild thermal environment forces this phase transition on anatase TiO_2 nanocrystals with size bigger than 12 nm, and transforms anatase TiO_2 into Li_1TiO_2 . Since the lithium intercalation path of the 2nd phase transition is significantly smaller than the 1st phase transition (O-O interatomic distance of $\text{TiO}_2 \rightarrow 3.08 - 3.77$ angstrom and $\text{Li}_1\text{TiO}_2 \rightarrow 2.96$ angstrom) (Figure 2.3.12), the anomalous phase transition to Li_1TiO_2 on 12 nm-

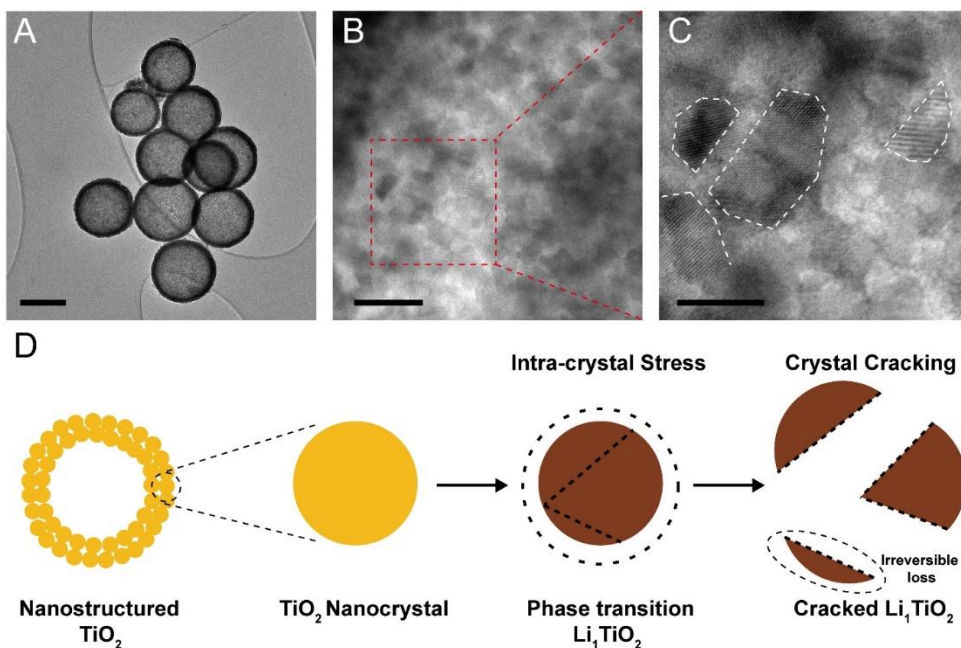


Figure 2.3.18. Representative Cs-corrected STEM images of 12 NT after the 20th lithium intercalation cycle at 60 °C (point v in Figure 2.3.17.C). A) Low magnification and B) high magnification bright field (BF)-STEM image of cracked anatase TiO₂ crystals after 20th cycling. C) Higher magnified BF-STEM image of a region marked by square in Figure 2.3.18.B (scale bar, (A) 200 nm, (B) 20 nm, and (C) 10 nm). D) Schematic of battery aging through intra-crystal stress generation and subsequent crystal cracking during lithium intercalation in mild thermal condition.

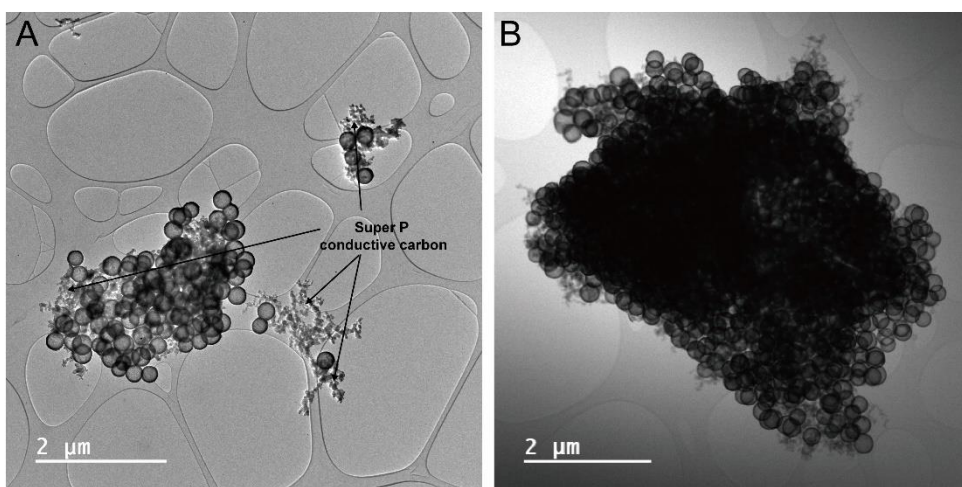


Figure 2.3.19. Low magnification TEM and STEM images of 12 NT after the 20th lithium intercalation cycle at 60 °C. Nanostructures are well preserved.

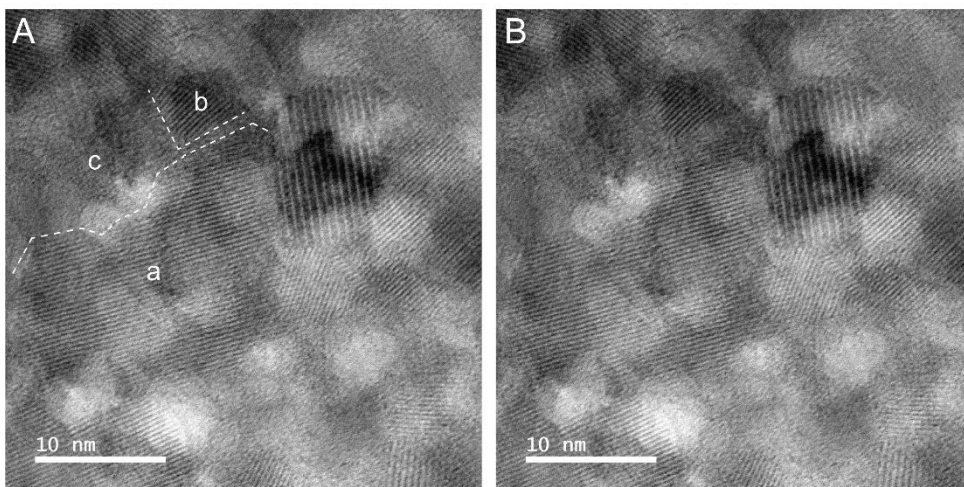


Figure 2.3.20. High magnification BF-STEM images of 12 NT after the 20th lithium intercalation cycle at 60 °C. In A), a, b and c compose initial anatase TiO₂ crystal. White dotted line guides abrupt crystal interface. c part is missing upon continuous cycling. For comparison, identical image is shown on B) without figure legends.

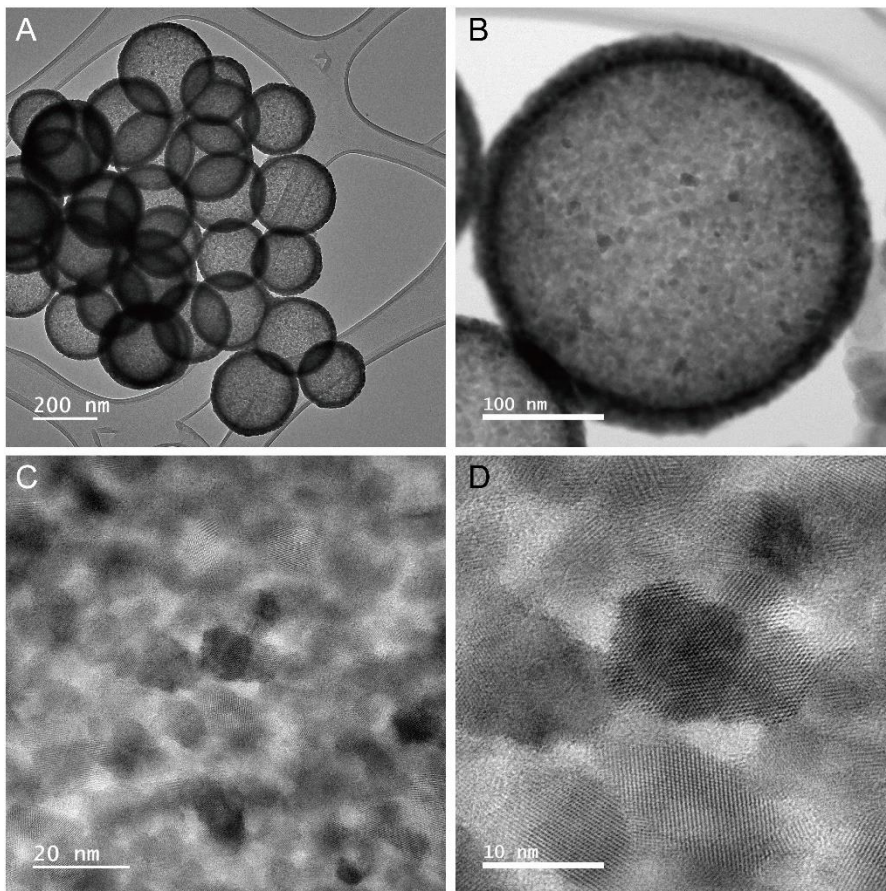


Figure 2.3.21. Cs-corrected BF-STEM images of 12 NT after the 20th lithium intercalation cycle at RT.

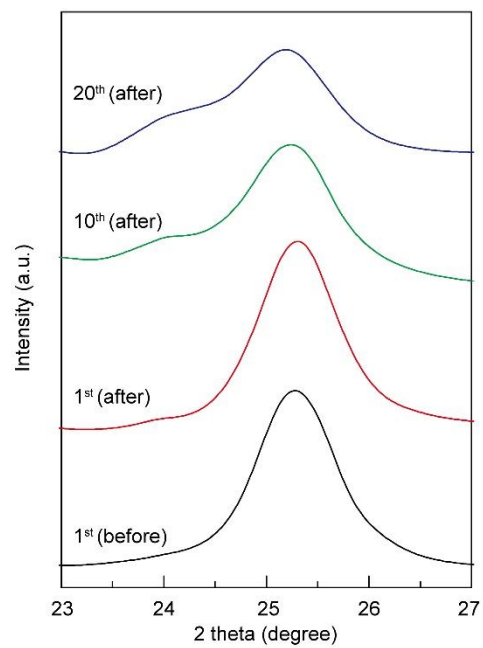


Figure 2.3.22. XRD patterns of 12 NT before the test and after the 1st, 10th and 20th lithium intercalation cycle at 60 °C.

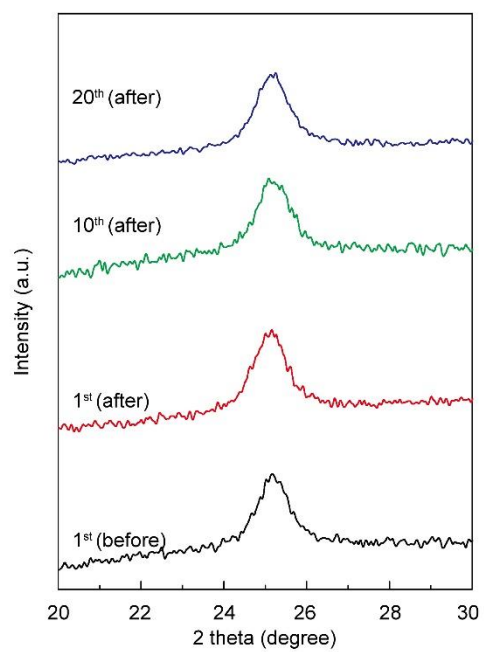


Figure 2.3.23. XRD patterns of 12 NT before the test and after the 1st, 10th and 20th lithium intercalation cycle at RT.

sized anatase TiO₂ generates severe intra-crystal stress. Subsequently, the excess-lithium intercalated TiO₂ nanocrystals alleviate the generated intra-crystal stress by forming fragmented crystals (Figure 2.3.18D). Since Li₁TiO₂ possesses significantly lower lithium diffusion coefficient compared to anatase TiO₂ or Li_{0.5}TiO₂ (see detailed explanation in Figure 2.3.12),⁴⁴ low lithium diffusion coefficient in Li₁TiO₂ crystals and poor grain-to-grain connection through crystal cracking accelerates the permanent loss of active materials (in the form of Li₁TiO₂) upon cycling. Notably, incomplete delithiation (irreversible Li ion trapping) is already observed as Li₁TiO₂ residue after the 1st cycle, which is rapidly accumulated as cycle number increases (Figure 2.3.22). Voltage profiles obtained at 60 °C also show the accumulation of permanent Li trapping. After the delithiation in 1st cycle, 30% of intercalated Li ions are trapped/irreversible. In the subsequent cycles, 13%, 8% and 7% of Li ions were additionally trapped at the 2nd, 10th and 20th cycle, respectively (Figure 2.3.24). Thus, the Li trapping accumulates as cycle proceeds, which can be observed as distinct shoulder peak (Li₁TiO₂, around 24°) growth in *operando* XRD patterns upon cycling (1st, 10th, and 20th cycle in Figure 2.3.22). Thus, the crystal cracking observed in the mild thermal environment is induced by unwanted phase transition to Li₁TiO₂ through excess lithium intercalation, which is distinctively different from simply downsizing constituent nanocrystals. Fragmentation of intra-granular crystals and irreversible intercalation of lithium ions in the crystal lattice in various electrode materials have been suggested as the main causes for battery aging.^{5-9,22,23,42,43}

The battery behavior of degraded electrode was examined at different rates (lower current rates in particular) to evaluate the lithium storage kinetics of the active materials. To start, we degraded the electrode under battery operation at 90 °C (100 mA g⁻¹) until the voltage plateau at 1.75 V significantly diminishes (Figure 2.3.25.A). When the degraded electrode was cycled on 50 mA g⁻¹, 25 mA g⁻¹, and 10 mA g⁻¹, the capacity was partly recovered. While initially degraded electrode exhibited the

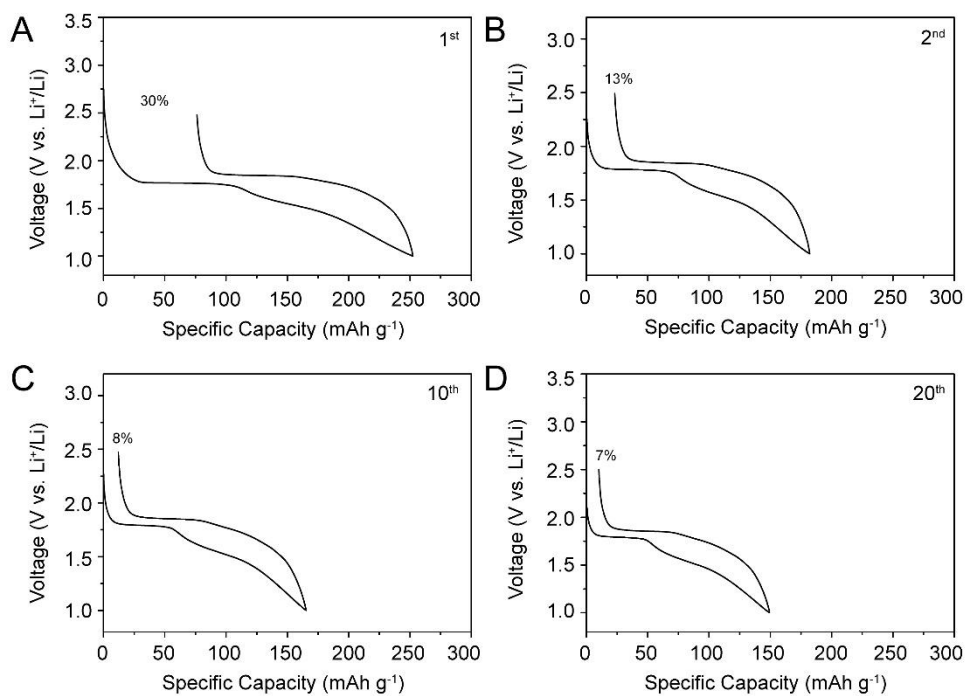


Figure 2.3.24. Voltage profiles of 12 NT after (A) 1st, (B) 2nd, (C) 10th and (D) 20th lithium intercalation cycle at 60 °C. The irreversible Li loss accounts 30%, 13%, 8%, and 7% on the 1st, 2nd, 10th, and 20th cycle, respectively.

capacity of 57.3 mAh g⁻¹ at 100 mA g⁻¹, the capacities at the lower rates at the identical temperature were increased to 70.1 mAh g⁻¹ at 50 mA g⁻¹, 80.2 mAh g⁻¹ at 25 mA g⁻¹, and 114.5 mAh g⁻¹ at 10 mA g⁻¹, respectively (Fig. S22B). Importantly, the capacity on the voltage plateau at 1.75 V (TiO₂ → Li_{0.55}TiO₂) was not recovered, while most of the recovered capacity is attributed to low voltage slope region where the second phase transition takes place (Li_{0.55}TiO₂ → Li₁TiO₂) (Figure. 2.3.25.B). This result indicates the ‘*lithium intercalation induced crystal cracking*’ generates electrochemically dead part. First, the irreversible capacity loss from the voltage plateau at 1.75 V indicates that once the cracked Li₁TiO₂ particles lose the electrical contact from the current collector, it can not go back to initial anatase TiO₂ and accumulates as the electrochemically dead part. Thus, poor grain-to-grain connection resulted from the ‘*lithium intercalation induced crystal cracking*’ generates electrochemically dead part, and the Li₁TiO₂ in this electrochemically dead part accumulates and leads to permanent Li loss. Second, the partial recovery of the capacity in the lower voltage slope region (Figure 2.3.25.B) indicates the lithium diffusion in the Li₁TiO₂ particles in electrochemically active part is kinetically hindered, but still can be recovered through lowering the cycling rate. However, the recovered capacity takes only a small portion of the initial capacity, which indicate the performance loss of battery aging in mild-thermal environment is majorly from permanent Li loss.

Our results demonstrate that entire lithium intercalation chemistry can be affected even at near-ambient temperature (45 - 60 °C), complicating battery operation process. Since LIBs are typically combined with heat-generating devices, further investigations on the thermal environment should be carried out.

In Figure 6A, cycle performance summarizes the effects of battery aging on both short and long-term capacity at different temperatures (RT, 60 °C, 90 °C). In the 1st cycle, thermal condition accelerates extra lithium intercalation and leads to sequential phase transition, resulting in the higher lithium storage (218.6 mAh g⁻¹,

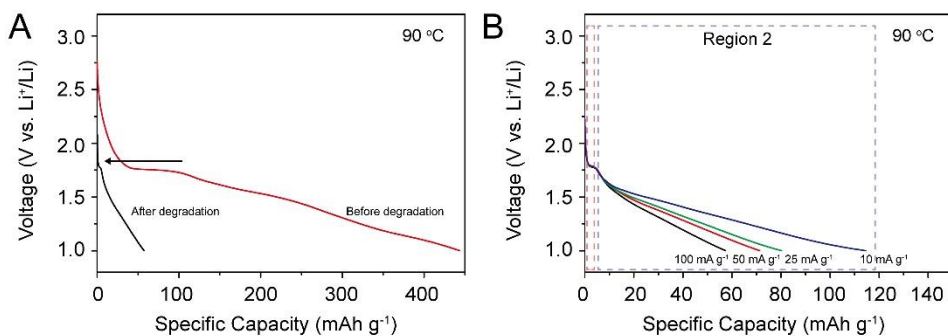


Figure 2.3.25. (A) Voltage profile comparison before and after the battery degradation (90 °C, 100 mA g⁻¹), and (B) voltage profiles of the degraded electrode at different rates (90 °C, 100 mA g⁻¹, 50 mA g⁻¹, 25 mA g⁻¹, and 10 mA g⁻¹). During the battery degradation, significant shortage of voltage plateau at 1.75 V is observed (A). The capacity in the lower voltage slope (region 2) was partially recovered under lower cycling rates, while capacity at 1.75 V plateau remained unchanged (B).

252.4 mAh g⁻¹ and 443.6 mAh g⁻¹ for RT, 60 °C and 90 °C). However, excess lithium storage has a long-term adverse effect, showing capacity reversal upon cycling. Compared to the capacity at RT, the capacity crossover occurs after the 21st cycle at 60 °C, which is accelerated at the higher temperature of 90 °C (6th cycle). As a result, the capacity after the 50th cycle at higher temperatures is much lower than that at RT (117.6 mAh g⁻¹, 51.3 mAh g⁻¹ and 23.5 mAh g⁻¹ for RT, 60 °C and 90 °C) (Fig. 6A).

Lastly, to investigate if the battery aging induced by the thermal condition can be recovered, we divided the battery operation condition into two parts: operation under 60 °C for the 1st to 20th cycle, and elimination of thermal condition and operate under RT for the 20th to 40th cycle (Fig. 6B). Two things are notable. First, the decreased performance on mild thermal environment is irreversible even when the heat is removed. Second, abrupt capacity reduction is observed right after the removal of heating (148.0 mAh g⁻¹ in 20th and 112.9 mAh g⁻¹ in 21st), due to the inhibited phase transition to Li₁TiO₂ at RT. Consequently, the experience of battery operation in mild thermal environment accumulates the unexpected lithium-excess Li₁TiO₂ phase upon cycling. Continuous experience in the unexpected sequential phase transition induces significant intra-crystal stress, leading to crystal cracking. This severe crystal fragmentation along with the accumulated Li₁TiO₂ phase results in dramatic capacity decay and irreversible capacity loss, thus the battery aging, even after the heat is removed.

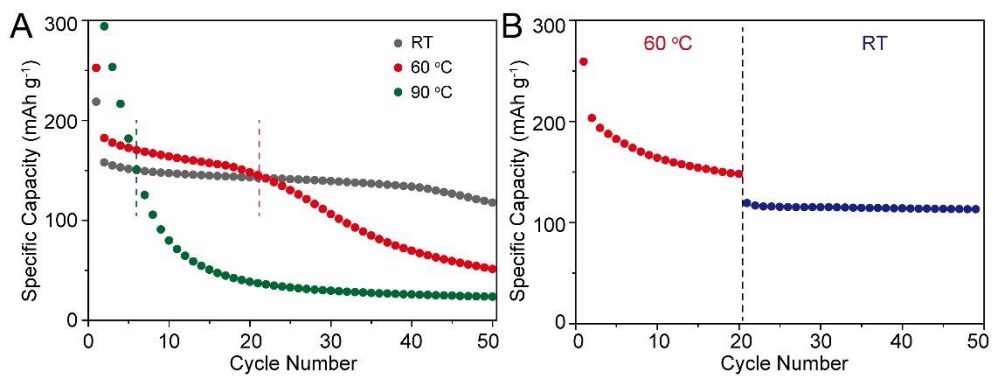


Figure 2.3.26. A) Cycle performance of 12 NT at a current density of 100 mA g⁻¹ at various temperature (RT, 60 °C, 90 °C). B) Cycle performance of 12 NT at 100 mA g⁻¹ through thermal condition change from 60 °C to RT after 20 cycles.

2.4. Conclusion

In this article, we investigated chemical and structural origin of Li-ion battery aging in mild thermal environment, using anatase TiO_2 as a model intercalation compound. Our result highlights that the thermal contribution can affect and change the entire lithium intercalation chemistry even at near-ambient temperature, suggesting proper attention is required for the future design of LIBs that operate in these conditions. In the case of anatase TiO_2 , the mild thermal environment induces unexpected sequential phase transition ($\text{TiO}_2 \rightarrow \text{Li}_{0.55}\text{TiO}_2 \rightarrow \text{Li}_1\text{TiO}_2$). The sequential phase transition has two distinct effects: capacity enhancement in the first few cycles, and accumulation of Li_1TiO_2 phase that leads to long-term battery aging. Through various experiments including *operando* measurements and Cs-STEM imaging, we provide rational explanations on how Li-ion battery aging initiates and proceeds in the mild thermal environment. Since most of the industrially important intercalation compounds (graphite, LiCoO_2 , LiMnO_2 , $\text{Li}(\text{Ni,Mn,Co})\text{O}_2$) have previously shown to experience severe capacity decay through irreversible lithium intercalation in mild thermal environment, our results provide an important direction to investigate how the battery aging proceeds in various other materials.

2.5. References

- (1) Lu, J.; Chen, Z.; Ma, Z.; Pan, F.; Curtiss, L. A.; Amine, K. The Role of Nanotechnology in the Development of Battery Materials for Electric Vehicles. *Nat. Nanotech.* **2016**, *11*, 1031.
- (2) Sun, Y.; Liu, N.; Cui, Y. Promises and Challenges of Nanomaterials for Lithium-Based Rechargeable Batteries. *Nat. Energy* **2016**, *1*, 16071.
- (3) Bruce, P. G.; Scrosati, B.; Tarascon, J. M. Nanomaterials for Rechargeable Lithium Batteries. *Angew. Chem. Int. Ed.* **2008**, *47*, 2930.
- (4) Choi, J.; Aurbach, D. Promise and Reality of Post-Lithium-Ion Batteries with High Energy Densities. *Nat. Rev. Mater.* **2016**, *1*, 16013.
- (5) Ramadass, P.; Haran, B.; White, R.; Popov, B. N. Capacity Fade of Sony 18650 Cells Cycled at Elevated Temperatures: Part I. Cycling Performance. *J. Power Sources* **2002**, *112*, 606.
- (6) Ma, S.; Jiang, M.; Tao, P.; Song, C.; Wu, J.; Wang, J.; Deng, T.; Shang, W. Temperature Effect and Thermal Impact in Lithium-Ion Batteries: A Review. *Pro. Nat. Sci-Mater.* **2018**, *28*, 653.
- (7) Markevich, E.; Pollak, E.; Salitra, G.; Aurbach, D. On the Performance of Graphitized Meso Carbon Microbeads (MCMB)–Meso Carbon Fibers (MCF) and Synthetic Graphite Electrodes at Elevated Temperatures. *J. Power Sources* **2007**, *174*, 1263.
- (8) Gabrisch, H.; Ozawa, Y.; Yazami, R. Crystal Structure Studies of Thermally Aged LiCoO_2 and LiMn_2O_4 Cathodes. *Electrochim. Acta* **2006**, *52*, 1499.
- (9) Bodenes, L.; Naturel, R.; Martinez, H.; Dedryvere, R.; Menetrier, M.; Croguennec, L.; Peres, J. P.; Tessier, C.; Fischer, F. Lithium Secondary Batteries Working at Very High Temperature: Capacity Fade and Understanding of Aging Mechanisms. *J. Power Sources* **2013**, *236*, 265.

- (10) Wagemaker, M.; Borghols, W. J. H.; Mulder, F. M. Large Impact of Particle Size on Insertion Reactions. A Case for Anatase Li_xTiO_2 . *J. Am. Chem. Soc.* **2007**, *129*, 4323.
- (11) Yahia, M. B.; Vergnet, J.; Saubanere, M.; Doublet, M. L. Unified Picture of Anionic Redox in Li/Na-Ion Batteries. *Nat. Mater.* **2019**, *18*, 496.
- (12) Lee, J.; Kitchaev, D. A.; Kwon, D. H.; Lee, C. W.; Papp, J. K.; Liu, Y. S.; Lun, Z.; Clément, R. J.; Shi, T.; McCloskey, B. D.; Guo, J.; Balasubramanian, M.; Ceder, G. Reversible $\text{Mn}^{2+}/\text{Mn}^{4+}$ Double Redox in Lithium-Excess Cathode Materials. *Nature* **2018**, *556*, 185.
- (13) Lim, J.; Li, Y.; Alsem, D. H.; So, H.; Lee, S. C.; Bai, P.; Cogswell, D. A.; Liu, X.; Jin, N.; Yu, Y. S.; Salmon, N. J.; Shapiro, D. A.; Bazant, M. Z.; Tylliszczak, T.; Chueh, W. C. Origin and Hysteresis of Lithium Compositional Spatiodynamics within Battery Primary Particles. *Science* **2016**, *353*, 566.
- (14) Gibot, P.; Casas-Cabana, M.; Laffont, L.; Levasseur, S.; Carlach, P.; Hamelet, S.; Tarascon, J. M.; Masquelier, C. Room-Temperature Single-Phase Li Insertion/Extraction in Nanoscale Li_xFePO_4 . *Nat. Mater.* **2008**, *7*, 741.
- (15) Wagemaker, M.; Mulder, F. M. Properties and Promises of Nanosized Insertion Materials for Li-Ion Batteries. *Acc. Chem. Res.* **2013**, *46*, 1206.
- (16) Augustyn, V.; Come, J.; Lowe, M. A.; Kim, J. W.; Taberna, P. L.; Tolbert, S. H.; Abruna, H. D.; Simon, P.; Dunn, B. High-Rate Electrochemical Energy Storage through Li^+ Intercalation Pseudocapacitance. *Nat. Mater.* **2013**, *12*, 518.
- (17) Tavassol, H.; Jones, E. M. C.; Sottos, N. R.; Gewirth, A. A. Electrochemical Stiffness in Lithium-Ion Batteries. *Nat. Mater.* **2016**, *15*, 1182.
- (18) Pikul, J. H.; Zhang, H. G.; Cho, J.; Braun, P. V.; King, W. P. High-Power Lithium Ion Microbatteries from Interdigitated Three-Dimensional Bicontinuous Nanoporous Electrodes. *Nat. Commun.* **2013**, *4*, 1732.

- (19) Zhang, J. N.; Li, Q.; Ouyang, C.; Yu, X.; Ge, M.; Huang, X.; Hu, E.; Ma, C.; Li, S.; Xiao, R.; Yang, W.; Chu, Y.; Liu, Y.; Yu, H.; Yang, X. Q.; Huang, X.; Chen, L.; Li, H. Trace Doping of Multiple Elements Enables Stable Battery Cycling of LiCoO_2 at 4.6 V. *Nat. Energy* **2019**, *4*, 594.
- (20) Lee, D. H.; Lee, B. H.; Sinha, A. K.; Park, J. H.; Kim, M. S.; Park, J.; Shin, H.; Lee, K. S.; Sung, Y.; Hyeon, T. Engineering Titanium Dioxide Nanostructures for Enhanced Lithium-Ion Storage. *J. Am. Chem. Soc.* **2018**, *140*, 16676.
- (21) Ren, D.; Padgett, E.; Yang, Y.; Shen, L.; Shen, Y.; Levin, B. D. A.; Yu, Y.; DiSalvo, F. J.; Muller, D. A.; Abruna, H. D. Ultrahigh Rate Performance of a Robust Lithium Nickel Manganese Cobalt Oxide Cathode with Preferentially Oriented Li-Diffusing Channels. *ACS Appl. Mater. Interfaces* **2019**, *11*, 41178.
- (22) Yan, P.; Zheng, J.; Gu, M.; Xiao, J.; Zhang, J. G.; Wang, C. M. Intragranular Cracking as a Critical Barrier for High-Voltage Usage of Layer-Structured Cathode for Lithium-Ion Batteries. *Nat. Commun.* **2017**, *8*, 14101.
- (23) Yan, P.; Zheng, J.; Liu, J.; Wang, B.; Cheng, X.; Zhang, Y.; Sun, X.; Wang, C.; Zhang, J. G. Tailoring Grain Boundary Structures and Chemistry of Ni-Rich Layered Cathodes for Enhanced Cycle Stability of Lithium-Ion Batteries. *Nat. Energy* **2018**, *3*, 605.
- (24) Wagemaker, M.; Kentgens, A. P. M.; Mulder, F. M. Equilibrium Lithium Transport Between Nanocrystalline Phases in Intercalated TiO_2 Anatase. *Nature* **2002**, *418*, 397.
- (25) Zhu, G. N.; Wang, Y. G.; Xia, Y. Y. Ti-Based Compounds as Anode Materials for Li-Ion Batteries. *Energy Environ. Sci.* **2012**, *5*, 6652.
- (26) Ye, J.; Liu, W.; Cai, J.; Chen, S.; Zhao, X.; Zhou, H.; Qi, L. Nanoporous Anatase TiO_2 Mesocrystals: Additive-Free Synthesis, Remarkable Crystalline-Phase Stability, and Improved Lithium Insertion Behavior. *J. Am. Chem. Soc.* **2011**, *133*, 933.

- (27) Niu, P.; Wu, T.; Wen, L.; Tan, J.; Yang, Y.; Zheng, S.; Liang, Y.; Li, F.; Irvine, J. T. S.; Liu, G.; Ma, X.; Cheng, H. M. Substitutional Carbon-Modified Anatase TiO₂ Decahedral Plates Directly Derived from Titanium Oxalate Crystals via Topotactic Transition. *Adv. Mater.* **2018**, *30*, 1705999.
- (28) Lee, B. H.; Park, S.; Kim, M.; Sinha, A. K.; Lee, S. C.; Jung, E.; Chang, W. J.; Lee, K. S.; Kim, J. H.; Cho, S. P.; Kim, H.; Nam, K. T.; Hyeon, T. Reversible and Cooperative Photoactivation of Single-Atom Cu/TiO₂ Photocatalysts. *Nat. Mater.* **2019**, *18*, 620.
- (29) Gordon, T. R.; Cargnello, M.; Paik, T.; Mangolini, F.; Weber, R. T.; Fornasiero, P.; Murray, C. B. Nonaqueous Synthesis of TiO₂ Nanocrystals using TiF₄ to Engineer Morphology, Oxygen Vacancy Concentration, and Photocatalytic Activity. *J. Am. Chem. Soc.* **2012**, *134*, 6751.
- (30) Ren, H.; Sun, J.; Yu, R.; Yang, M.; Gu, L.; Liu, P.; Zhao, H.; Kisailus, D.; Wang, D. Controllable Synthesis of Mesostructures from TiO₂ Hollow to Porous Nanospheres with Superior Rate Performance for Lithium Ion Batteries. *Chem. Sci.* **2016**, *7*, 793.
- (31) Liu, H.; Li, W.; Shen, D.; Zhao, D.; Wang, G. Graphitic Carbon Conformal Coating of Mesoporous TiO₂ Hollow Spheres for High-Performance Lithium Ion Battery Anodes. *J. Am. Chem. Soc.* **2015**, *137*, 13161.
- (32) Wang, Z.; Zhou, L.; Lou, X. W. Metal Oxide Hollow Nanostructures for Lithium-ion Batteries. *Adv. Mater.* **2012**, *24*, 1903.
- (33) Lai, X.; Halpert, J. E.; Wang, D. Recent Advances in Micro-/Nano-Structured Hollow Spheres for Energy Applications: From Simple to Complex Systems. *Energy Environ. Sci.* **2012**, *5*, 5604.
- (34) Wang, X.; Feng, J.; Bai, Y.; Zhang, Q.; Yin, Y. Synthesis, Properties, and Applications of Hollow Micro-/Nanostructures. *Chem. Rev.* **2016**, *116*, 10983.

- (35) Jiang, C.; Wei, M.; Qi, Z.; Kudo, T.; Honma, I.; Zhou, H. Particle Size Dependence of the Lithium Storage Capability and High Rate Performance of Nanocrystalline Anatase TiO₂ Electrode. *J. Power Sources* **2007**, *166*, 239.
- (36) Du, J.; Lai, X.; Yang, N.; Zhai, J.; Kisalius, D.; Su, F.; Wang, D.; Jiang, L. Hierarchically Ordered Macro-Mesoporous TiO₂-Graphene Composite Films: Improved Mass Transfer, Reduced Charge Recombination, and Their Enhanced Photocatalytic Activities. *ACS Nano* **2011**, *5*, 590.
- (37) Joo, J. B.; Lee, I.; Dahl, M.; Moon, G. D.; Zaera, F.; Yin, Y. Controllable Synthesis of Mesoporous TiO₂ Hollow Shells: Toward an Efficient Photocatalyst. *Adv. Funck. Mater.* **2013**, *23*, 4246.
- (38) Kim, G.; Jo, C.; Kim, W.; Chun, J.; Yoon, S.; Lee, J.; Choi, W. TiO₂ Nanodisks Designed for Li-Ion Batteries: A Novel Strategy for Obtaining an Ultrathin and High Surface Area Anode Material at the Ice Interface. *Energy Environ. Sci.* **2013**, *6*, 2932.
- (39) Liu, H.; Joo, J. B.; Dahl, M.; Fu, L.; Zeng, Z.; Yin, Y. Crystallinity Control of TiO₂ Hollow Shells through Resin-Protected Calcination for Enhanced Photocatalytic Activity. *Energy Environ. Sci.* **2015**, *8*, 286.
- (40) Aricò, A. S.; Bruce, P.; Scrosati, B.; Tarascon J. M.; van Schalkwijk, W. Nanostructured Materials for Advanced Energy Conversion and Storage Devices. *Nat. Mater.* **2005**, *4*, 366.
- (41) Shin, J. Y.; Samuelis, D.; Maier, J. Sustained Lithium-Storage Performance of Hierarchical, Nanoporous Anatase TiO₂ at High Rates: Emphasis on Interfacial Storage Phenomena. *Adv. Funct. Mater.* **2011**, *21*, 3464.
- (42) Shi, F.; Song, Z.; Ross, P. N.; Somorjai, G. A.; Ritchie, R. O.; Komvopoulos, K. Failure Mechanisms of Single-Crystal Silicon Electrodes in Lithium-Ion Batteries. *Nat. Commun.* **2016**, *7*, 11886.
- (43) Tavassol, H.; Cason, M. W.; Nuzzo, R. G.; Gewirth, A. A. Influence of Oxides

on the Stress Evolution and Reversibility during SnO_x Conversion and Li-Sn Alloying Reactions. *Adv. Energy Mater.* **2015**, *5*, 1400317.

(44) Belak, A. A.; Wang, Y.; Van der Ven, A. Kinetics of Anatase Electrodes: The Role of Ordering, Anisotropy, and Shape Memory Effects. *Chem. Mater.* **2012**, *24*, 2894.

Chapter 3. Bi-MOF Derived Micro/Meso-Porous Bi@C Nanoplates for High Performance Lithium-Ion Batteries

Note: Studies on this part was written based on, and figures are based on the work conducted with Min-Kun Kim(co-first author), published in *Nanoscale* **2020**, *12*, 15214

3.1. Introduction

For a long time, lithium ion batteries (LIBs) have been considered as the most attractive energy storage systems for small electric devices and electric vehicles owing to their low cost, long life spans, and high energy density.¹⁻³ In recent years, the demand for LIBs with higher energy density and longer life spans has been increasing due to the development of high-performance electronic devices and the introduction of electric vehicles.⁴⁻⁸ However, the currently used carbon-based anode materials are unable to meet these demand owing to their low theoretical (372 mAh g⁻¹) and volumetric capacity (840 mAh cm⁻³).⁹⁻¹³ In order to replace graphite-based anode materials, there have been extensive efforts to find alternative materials among transition metals, post-transition metals, and metalloids.¹⁴⁻²⁰ In particular, metalloids and post-transition metals have been attracting attention as potential anode materials owing to their high theoretical capacity and volumetric capacity. In terms of theoretical capacity, for example, silicon, one of the metalloid group material, has high theoretical capacity of 3579 mAh g⁻¹.^{21,22} and Sn, one of the post-transition metal group material, has a theoretical capacity of 993 mAh g⁻¹.²³ In addition, Sb (660 mAh g⁻¹) and Ge (1624 mAh g⁻¹) also have high theoretical capacities.²⁴⁻²⁶ Although bismuth has lower theoretical capacity (386 mAh g⁻¹) than other post-transition metals, it has a very high theoretical volumetric capacity (3765 mAh cm⁻³

³), which is higher than that of Si (2190 mAh cm⁻³).²⁷⁻²⁹ This advantageous feature is very effective for electric vehicles, which require high energy density in a limited space. Therefore, numerous researchers have studied bismuth and its compounds for application in energy storage systems.³⁰⁻³⁶ Moreover, the crystalline structure of bismuth has a long distance along the c-axis, which makes lithium ions highly accessible to it.³⁷⁻³⁸ Accordingly, the potential hysteresis of bismuth, that is, the potential difference between lithiation and delithiation, is lower than those of other lithium alloying metals.^{39,40} Despite these advantages, similar to the case of other metals or metal oxides, alloying with lithium during cycling causes high volume expansion (~215%) and pulverization of the Bi-based electrode.⁴¹⁻⁴³ Although bismuth is classified as a metal, it has a rather low electrical conductivity. To overcome these issues, researchers have attempted to prepare composites of Bi with carbon materials. Carbon or a carbon-based composite material used as an additive can reduce the pulverization effects due to volume expansion. Moreover, to increase the electrical conductivity, various methods of carbon coating on nanoparticles have been studied or highly conductive materials such as graphene and carbon nanotubes have been incorporated into the electrode. For example, Dai et al. prepared carbon-coated mesoporous bismuth nanowires from Bi₂S₃ nanowires. Cavities formed in the Bi@C nanowire via the pyrolysis of Bi₂S₃ modulated the volume expansion during cycling, and thus enhanced the stability of Li-ion cells (specific capacity of 408 mAh g⁻¹ after 100 cycles at 100 mA g⁻¹).³⁸ Zhang et al. engineered N-doped graphene/Bi nanocomposite for LIBs. N-doped graphene increased the electrical conductivity of Bi nanoparticles and alleviated volume expansion.³² In addition, synthetic studies on controlling the morphology of nanostructures have also been reported. For example, Lan et al. synthesized a rose-like Bi anode materials which exhibits high electrical properties by coating N-rich carbon on Bi. The nanostructure showed exceptional electrochemical properties (specific capacity of 535 mAh g⁻¹ after 450 cycles at 200 mA g⁻¹).³⁰

Herein, we present the facile preparation of Bi@C micro-nano complexed sheets obtained by the pyrolysis of Bi-based metal-organic frameworks (MOFs). MOFs are well known as novel 3-D porous materials consisting of ordered networks of metal clusters and organic linkers. Also, MOFs having excellent metal distributions in the carbonaceous matrix is an ideal substance for volume changing alloying type negative electrode. After Yaghi et al. named this porous material as MOFs, tens of thousands of MOFs have been developed.⁴⁴ Interesting characteristics of MOFs, such as a large surface area ranging up to $7,000 \text{ m}^2 \text{ g}^{-1}$,⁴⁵ catalytic effects,⁴⁶⁻⁵³ and varying structure, which can be tailored, have attracted the attention of many researchers.⁵⁴ ⁵⁶ In some cases, there have been attempts to apply MOF-based materials to energy devices.^{57-62,76} In this study, we modified the previously reported synthesis of Bi-based MOFs⁶³ and subsequently pyrolyzed the Bi-based MOFs under inert condition. After carbonization, Bi-metal clusters are transformed into Bi nanoparticles encompassed by a carbon shell. Additionally, the pyrolysis of Bi-based MOFs gives rise to interesting micro/meso-porous structures, which facilitate contact between the electrode and electrolyte, and thus enhance the cell performance. These distinct features of Bi@C, achieved by the synthesis of a 2D carbon-shelled nano-plate containing Bi nanoparticles by a simple method, led to enhanced lithium storage performance and excellent cycle performance of the Bi@C anode in LIBs. The lithium storage performance was highly improved from the other reported Bi@C composites (Table 3.1.1).

Materials	Current density (mA g⁻¹)	Cycle numbers	Capacity (mAh g⁻¹)	References
Nanostructured bismuth-based composites	100	100	300	<i>J. Power Sources</i> , 2009, 186 , 206
Bismuth/CNF anodes	100	200	484	<i>Nanoscale</i> , 2017, 9 , 13298
Bi@C core-shell nanowires	100	100	408	<i>Nanoscale</i> , 2014, 6 , 13236
Bi@C nanoplates	150	150	605	<i>ChemistrySelect</i> , 2018, 3 , 8973
Bi Nanoparticles anchored in N-doped porous carbon	80	100	285	<i>Nano-Micro Lett.</i> , 2018, 10 , 56,
N-doped graphene/Bi nanocomposites	50	10	390	<i>Ionics</i> , 2017, 23 , 1407
Micro/meso-porous Bi@C nanoplates	100	100	556	This work

Table 3.1.1 Comparison of Li storage performance on recent Bi@C composites

3.2. Experimental

Materials.

Bismuth nitrate pentahydrate [$\text{Bi}(\text{NO}_3)_3 \cdot 5\text{H}_2\text{O}$, 98%], benzene-1,3,5-tricarboxylic acid (H_3BTC , 95%), *N,N*-dimethylformamide (DMF, 99.8%), methanol (99.9%), bismuth metal (Bi, 99.9%, for comparison, Figure 3.3.16), and polyvinylidene fluoride (PVDF, Mw of 534,000) were purchased from Sigma-Aldrich and used without further purification.

Preparation of Bi-based MOFs.

First, we prepared Bi-based MOFs by a microwave-assisted synthesis method. This microwave-assisted synthesis is based on a previously reported hydrothermal process for the synthesis of Bi-MOFs.⁶³ In a typical process, $\text{Bi}(\text{NO}_3)_3 \cdot 5\text{H}_2\text{O}$ (0.472 g, 0.98 mmol) and H_3BTC (0.386 g, 1.84 mmol) were dissolved in 20 mL of DMF/methanol (1:3). After 20 min of sonication, the solution was transferred to a Teflon bottle for microwave-assisted heat-treatment. The reaction mixture was reacted at 120 °C for 5 h in a microwave-oven reactor. The product, a white precipitate, was collected by centrifugation (4,000 rpm, 10 min) and washed twice with DMF and twice with methanol, and dried in a vacuum oven at 60 °C.

Preparation of Bi@C.

The dried powder, Bi-based MOF, was calcined at 600 °C for 5 min under N_2 atmosphere to enable the formation of Bi nanoparticles in a carbon shell. After carbonization, the black powder was cooled slowly under inert condition for 3 h. After the furnace was cooled to room temperature, the sample was removed carefully.

Material characterization.

The morphology and structure of materials were observed by field-emission scanning electron microscopy (FE-SEM; SUPRA 55VP (Carl Zeiss)) and

transmission electron microscopy (TEM; Tecnai F20, FEI) at 200 kV. The crystallinity of the materials was analyzed by X-ray diffraction (XRD) performed on a Bruker D-5005 diffractometer with Cu $K\alpha$ radiation. XRD patterns Bi@C were collected in the 2θ range of 10 to 80° . The X-ray was generated at the voltage and current of 40 kV and 200 mA, respectively. Thermogravimetric analysis (TGA; TA SDT Q600) was conducted in air to determine the content of bismuth in Bi@C. Brunauer–Emmett–Teller (BET) analysis was conducted with N_2 absorption-desorption isotherms obtained on Micromeritics ASAPTM2020 for surface area analysis.

Electrochemical measurements.

The electrochemical properties of Bi@C were evaluated in a CR2032 coin type cell. The working electrode was prepared with a slurry composed of 70% active material, 20% carbon (Super P), and 10% binder (PVDF). The slurry was casted on Cu foil by the doctor blade method and the electrode was dried in vacuum at 120°C for 8 h.

The coin cell was assembled with Li-foil and working electrode in an argon-filled glove box. The electrolyte is 1 M LiPF_6 in ethylene carbonate and diethyl carbonate (1:1 vol%). The electrochemical performance was tested using a WBCS3000 cycler, WonAtech, Korea. The galvanostatic charge/discharge process was carried out in the voltage range of 0.01–3.0 V. Cyclic voltammetry (CV) was carried out in the voltage range of 0.01–3.0 V at a scan rate of 0.1 mV s^{-1} . Electrochemical impedance spectroscopy (EIS) was performed in the frequency range of 100 kHz to 10 mHz with 10 mV AC amplitude.

***In situ* XRD measurements.**

To conduct transmission *in situ* XRD analysis, a customized coin cell with a hole in the center and a Cu mesh electrode was used to reduce the interference of the Cu substrate. *In situ* X-ray diffraction patterns were collected using Smartlab 9 kW (Rigaku, Japan) with Cu $K\alpha$ radiation (1.5406 \AA) during the charge-discharge

process. *In situ* cell was discharged and charged at a current density of 50 mA g⁻¹ in the same voltage range during the 1st and 2nd cycles. The change of diffraction patterns was measured between $2\theta = 20$ and 60° by the transmission mode and an XRD pattern was obtained at intervals of about 60 min.

3.3. Results and Discussion

The preparation process of Bi@C is illustrated in Figure 3.3.1. In the first step, white Bi-based MOFs were synthesized by a microwave-assisted hydrothermal method and Figure 3.3.2 shows that morphology of Bi-based MOFs is thin and long 2D micro-sized plates. Microwave helps complete the fabrication of MOFs at a much faster rate than that of a conventional hydrothermal synthesis. After the prepared sample was dried, Bi-based MOFs were calcined in inert condition to form carbon-shelled Bi nanocomposite micro/nanoplates. In order to prevent the oxidation of the material, the pyrolysis was carried out in inert gas condition and the product was maintained in inert condition until it was cooled to room temperature. The SEM images in Fig. 1a and 1b show the morphology of Bi@C. Figure 3.3.3.a shows that Bi@C has a thin layered structure, similar to the shell of a tree. Figure 3.3.3.b shows that each layer consists of a 2D-structured porous sheet in which bismuth particles are thought to be enclosed within a carbonized body. The gap or void between the carbon structures is approximately 100 to 200 nm. The porous structure enhances the migration of lithium ion by increasing the contact area between the electrolyte and electrode materials. For example, a microporous structure, such as metal foam or an inverse opal structure, is applied to the electrode supporting body to increase the contact area between the electrode and electrolyte.⁶⁴⁻⁶⁵ The porosity of the prepared material was determined from the N₂ adsorption and desorption isotherm in Figure 3.3.3.c. The surface area of Bi@C calculated by the BET analysis is 116 m² g⁻¹. N₂ adsorption isotherms revealed that meso- (at low P/P₀) and macro- (at high P/P₀) pores were well developed in Bi@C. The pore size distribution calculated by the Barrett-Joyner-Halenda (BJH) method is displayed in Figure 3.3.3.d. The calculation confirmed that Bi@C has a mesoporous structure with a uniform pore size of 9.7 nm. These results indicate that Bi@C has a hierarchical structure with macro- and meso-

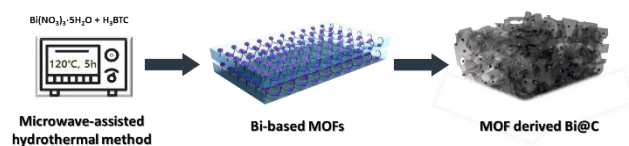


Figure 3.3.1 Schematic illustration of preparation of Bi@C

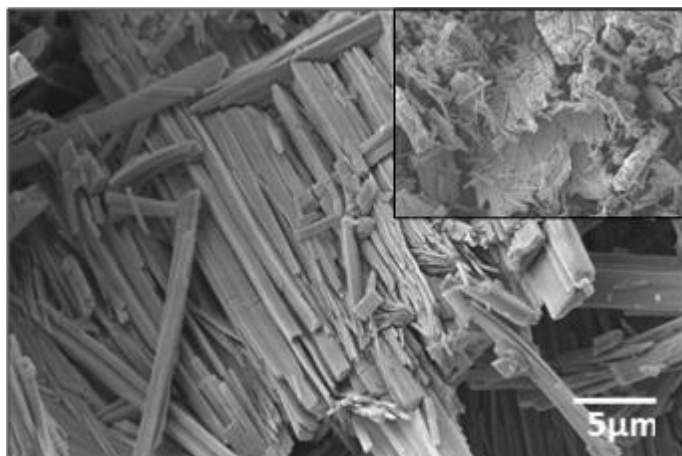


Figure 3.3.2 The SEM images of Bi-MOF after microwave-assisted hydrothermal method

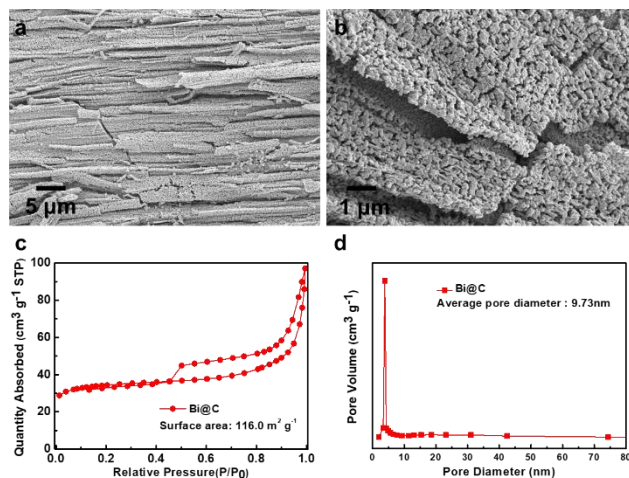


Figure 3.3.3 (a,b) SEM images of Bi@C after carbonization at different magnifications (c) N adsorption and desorption isotherm and (d) pore size distribution of Bi@C

pores and a large surface area. The TEM images of Bi@C in Figure 3.3.4.a and b show that bismuth nanoparticles derived from the metal clusters of Bi-based MOFs are evenly embedded in the micro/mesoporous carbon framework. The size of Bi nanoparticles dispersed in the carbon shell is diverse and ranges from 10 nm to 50 nm. In particular, the particles are not aggregated and are separated by 5 nm gaps across the carbon shell. The observed d-spacing value of (012) and (104) is 0.328 and 0.237 nm well matched with the previously reported articles (Figure 3.3.5).⁷⁶ Further, energy-dispersive X-ray spectroscopy (EDS) was performed to confirm the composition of the nanoparticles and carbon shell in Bi@C (see Figure 3.3.4.c and d). The results of the EDS analysis clearly confirm that the nanoparticles are composed of Bi and the shell covering the Bi nanoparticles is carbon. The contents of Bi and C were determined to be 74 and 24%, respectively, from the EDS analysis. We also confirmed the results by TGA analysis. As observed in the TGA curve (Fig. 3.3.6), there was a rapid decrease in mass between 300 and 400 °C, due to the oxidation of the carbon shell.⁶⁶ The slight increase in mass before the decomposition of carbon is due to the oxidation of Bi metal to Bi₂O₃.³⁰ XRD analyses were performed to confirm the crystal structure of the nanoparticles in Bi@C. In the XRD pattern of Bi@C (Figure 3.3.7), several noticeable peaks are identified at 27.2, 37.9, 39.6, 48.7, and 56.0°, corresponding to the (012), (104), (110), (202), and (024) planes of hexagonal bismuth [JCPDS card no. 44-12460]. The broad peak from 20 to 30° can be assigned to the amorphous carbon shell resulting from the pyrolysis process.⁶⁷ The electrochemical properties of the micro/mesoporous Bi@C as an anode in LIBs are shown in Figure 3.3.8. CV profiles from the 1st to 3rd cycles in the range of 0.01–3.0 V (Li⁺/Li) (Figure 3.3.8.a) were analyzed at a scan rate of 0.1 mV s⁻¹. As shown in Figure 3.3.8.a, there are two redox couples at 0.59 V and 0.76 V during lithiation (cathodic process). These two peaks corresponding to lithiation are attributed to the alloying of Bi metal to produce LiBi and Li₃Bi, respectively.^{39,68} During delithiation (anodic process), one broad peak is observed at 0.93 V,

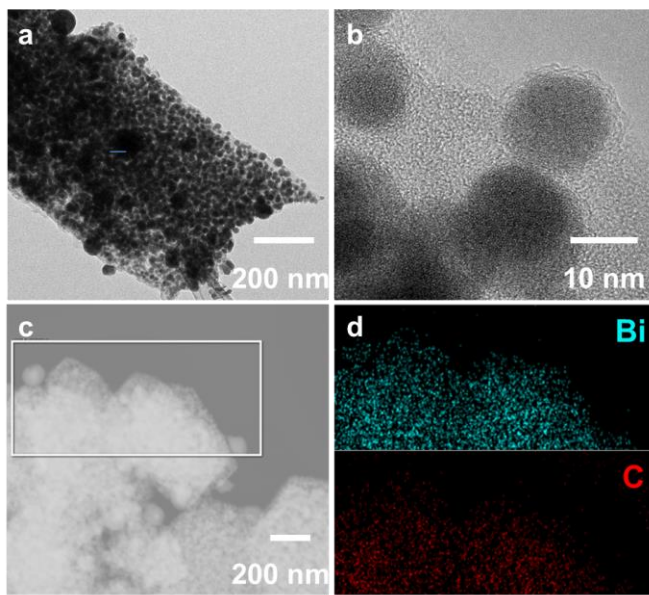


Figure 3.3.4 (a-c) TEM images of Bi@C after carbonization at different magnifications (d) EDS images of Bi@C

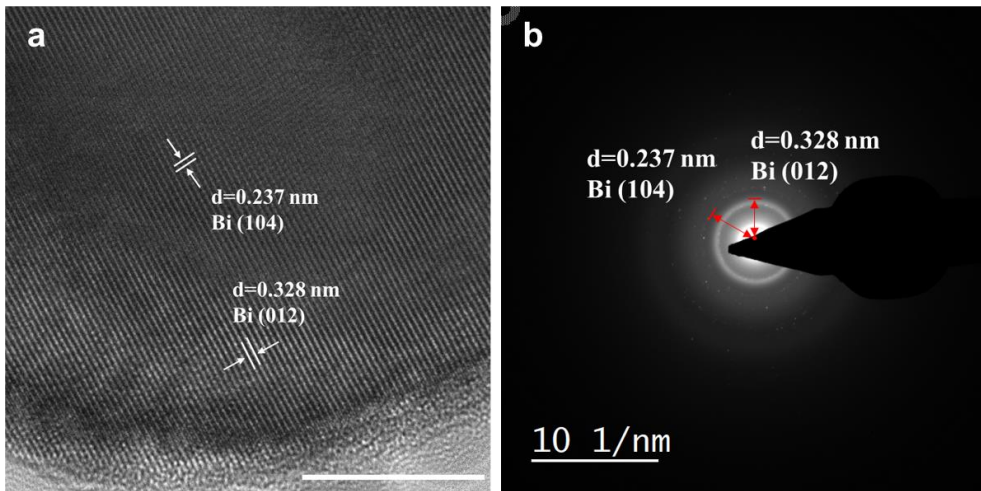
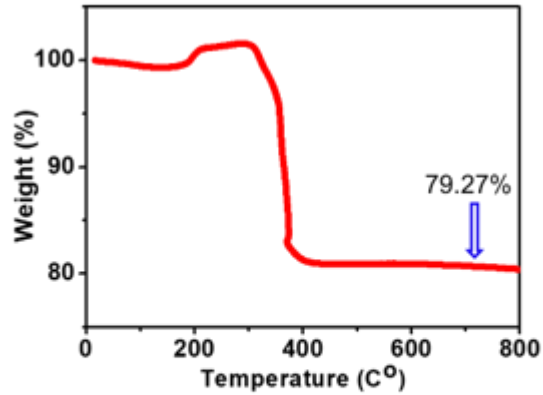


Figure 3.3.5 (a) TEM images and (b) SAED patterns of Bi@C (scale bar = 10nm)



$$\text{Bi (wt \%)} = 100 \times \frac{\text{Molecular weight of Bi} \times 2}{\text{Molecular weight of Bi}_2\text{O}_3} \times \frac{\text{Final weight of Bi}_2\text{O}_3}{\text{Initial weight of Bi/C}} = 71.7 \%$$

Molecular weight of Bi : 208.98 g mol⁻¹

Final weight of Bi₂O₃ : 3.183753 g

Molecular weight of Bi₂O₃ : 465.957 g mol⁻¹

Initial weight of Bi/C : 3.983276 g

Figure 3.3.6 Weight ratio measurement analysis of Bi@C by TGA

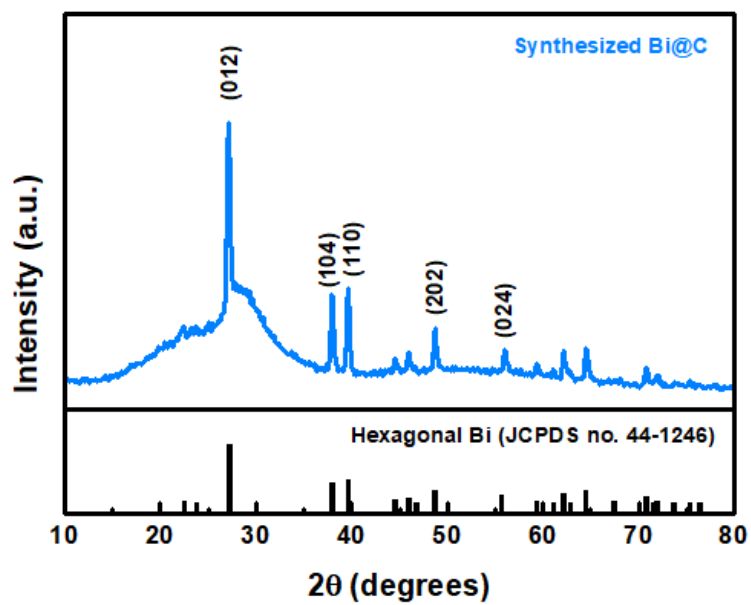


Figure 3.3.7 XRD patterns of Bi@C

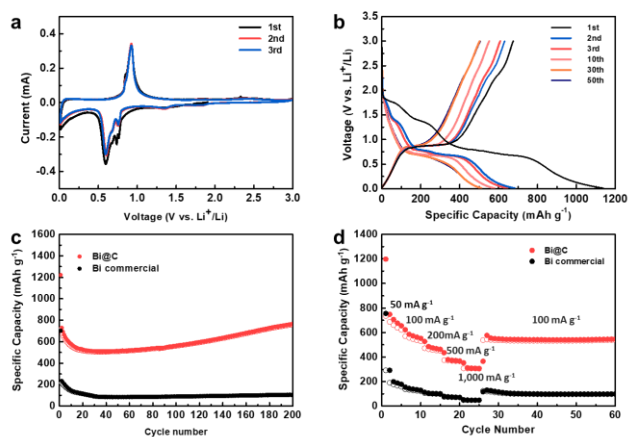


Figure 3.3.8 Electrochemical performance of the Bi@C (a) CV profiles of Bi@C for the first three cycles at a scan rate of 0.1 mV s^{-1} . (b) charge and discharge potential curves at 1,2,3,10,30,50 cycles. Lithium storage performance of the Bi@C and Bi commercial (c) cyclic performance at a current density of 100 mA g^{-1} . (d) C-rate performance at a current density of stepwise from 50 mA g^{-1} to 1000 mA g^{-1} .

corresponding to the reduction of the Li_3Bi alloy to Bi. The peak associated with the oxidation of Li appears as only one broad peak in contrast to the two reduction peaks. Xiaming et al. suggested that LiBi and Li_3Bi are oxidized in a very close voltage range during delithiation.³⁹ Except the first cycle, the CV profiles of the second and third cycles are totally overlapped in shape and intensity representing the high reversibility. For the 1st cycle, the initial extra current comparing to the subsequent cycles is thought to be originated from the formation of a solid electrolyte interphase (SEI) layer. On the other hand, as shown in Figure 3.3.9, the anode composed of commercial Bi showed peaks of oxidation and reduction that shifted during cycling. As a result, it can be inferred that the carbon shell increases the stability of the Li-ion cell. The charge/discharge potential curves of Bi@C at 1, 2, 3, 10, 30, and 50 cycles are displayed in Figure 3.3.8.b. In the first cycle, the discharge and charge capacities are 1139 and 675 mAh g⁻¹, respectively, with a Coulombic efficiency of 59% while Bi commercial shows lower Coulombic efficiency through the whole cycling performance (Figure 3.3.10). The low Coulombic efficiency during the first cycle is generally attributed to the formation of an SEI during the alloying or conversion reaction.^{69,70} In the initial three cycles, the voltage plateaus for redox couples are in good agreement with the results of CV. After 50 and 100 cycles, the voltage plateaus corresponding to the alloying reaction are maintained and the capacity of discharge is retained at 496 mAh g⁻¹ at a current density of 100 mA g⁻¹; however, the plateaus for the commercial Bi anode almost disappeared, as shown in Figure 3.3.11. The capacity of the commercial Bi anode degrades very rapidly and the reaction voltage plateau disappears after 20 cycles. In particular, the inset data shows that overpotential occurs between 10 and 20 cycles. As the charge and discharge processes proceeded, the resistance increased due to the byproducts generated on the surface of the particles from their side reaction with the electrolyte. However, it is presumed that the Bi@C carbon shell prevents the side reaction of Bi with the electrolyte and relieves the overpotential. In order to confirm the cycle stability specifically, the cycling performance of Bi@C at a current density of 100

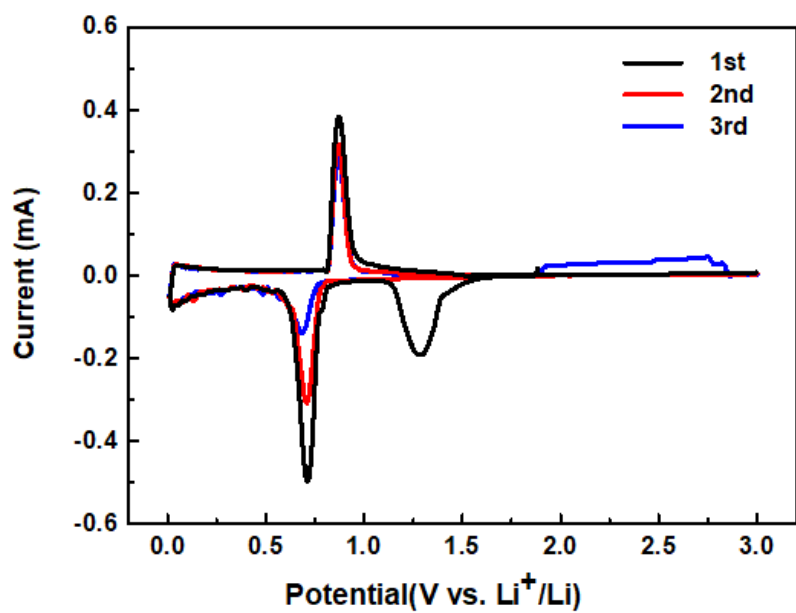


Figure 3.3.9 Electrochemical performance of CV profiles of Bi commercial for the first three cycles at a scan rate of 0.1 mV s^{-1}

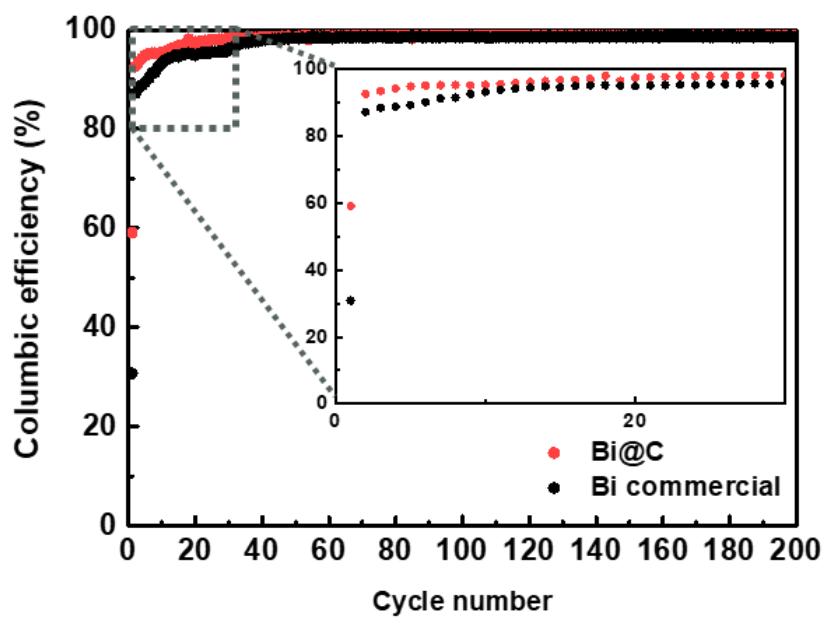


Figure 3.3.10 Coulombic efficiency of Bi@C and Bi commercial calculated from Figure 3.3.8

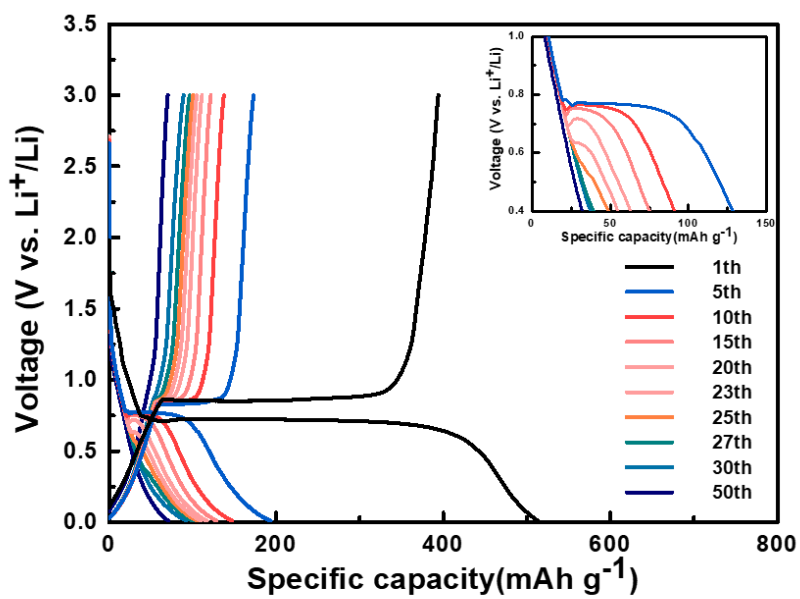


Figure 3.3.11 Charge and discharge potential curves of Bi commercial at a current density of 100 mA g⁻¹

mA g⁻¹ during 200 cycles was evaluated (Figure 3.3.8.c).

For comparison, the cycling performance of the anode composed of commercial Bi was also tested under the same conditions. The capacity of commercial Bi particle sharply dropped under 100 mA g⁻¹ before 30 cycles, while the capacity of the Bi@C anode was maintained at 556 mAh g⁻¹ over 100 cycles, and it consistently maintained excellent capacity over 200 cycles. The excellent cycle performance and stability of Bi@C are attributed to the carbon shell encapsulating the Bi nanoparticles, which inhibits pulverization of the anode materials due to volume expansion and induces the formation of a stable SEI.⁷¹ Moreover, the significantly enhanced capacity of Bi@C is attributed to the amorphous carbon shell, which acts as a conductive layer that effectively improves the electrical conductivity.⁷² In addition, metal nanoparticles in the carbon matrix exhibited extra capacity by catalyzing the conversion of SEI reversibly and thus leading to enhanced electrochemical performance.⁷³ In addition, it appears that the capacity gradually increases during the electrochemical process. Laruelle et al. described that the unusually high capacity results from the formation of a gel-like polymeric film on the anode material.⁷⁴ Electrodes under conversion and alloying reactions go through the activation process such as gradually wetting of the active materials by the electrolyte. It induces more electrochemically active sites available or structural rearrangement, which lead to enhanced utilization of the electrodes.⁷⁷ To confirm the structural stability of the Bi@C, SEM data is obtained at pristine and after 20 cycles of Bi@C and Bi commercial electrode (Figure 3.3.12). Pristine electrode images of Bi@C and Bi commercial is similar to the SEM images of each powder sample. (Figure 3.3.3.a, b and Figure 3.3.12). After 20 cycles, Bi commercial suffers severe cracking and pulverization upon cycling generating electrochemically dead part leading to rapidly degradation of the electrode.⁷⁵ Meanwhile, Bi@C shows superior maintenance of the initial 2D layered-porous structure.

This stable morphology can suppress the performance drop of the Bi@C electrode.

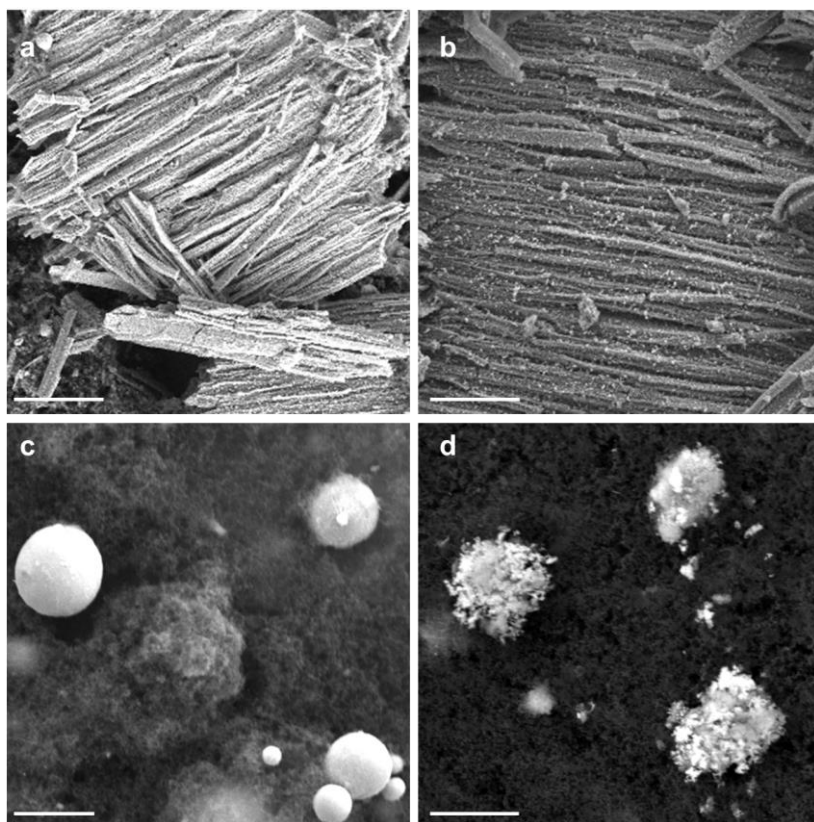


Figure 3.3.12 The SEM images of Bi@C electrode (a) pristine (b) after 20 cycles and Bi commercial electrode (c) pristine (d) after 20 cycles (scale bar = 10 μ m)

The mesoporous carbon matrix and nano-sized particles derived from the MOFs effectively improve the electrochemical performance at high C-rate. Figure 3.3.8.d shows the stepwise rate capability tests from 50 to 1000 mA g⁻¹, for every 5 cycles. The Bi@C showed good rate performance, with the capacities being 676, 562, 468, 366, and 308 mAh g⁻¹ at the current densities of 50, 100, 200, 500, and 1000 mA g⁻¹. After that, the specific capacity almost fully reverted to 554 mAh g⁻¹, when the current density rate was dropped to 100 mA g⁻¹. In the case of commercial Bi composed of micro-sized particles, the Li ions cannot fully infiltrate the interior parts of the giant particle at a high rate, and this kinetic resistance causes insufficient specific capacity.

In situ XRD analysis was investigated to elucidate the microscopic changes occurring in the materials during the lithiation and delithiation processes. Generally, according to the phase diagram, there are two phases for lithium-bismuth alloy, LiBi and Li₃Bi. The following two reactions occur during the electrochemical process:



Figure 3.3.13 demonstrates the phase changes during the electrochemical alloying reactions in the first and second cycles, as determined by *in situ* XRD. The peaks (36.6, 43.7, and 50.8°) that remain unchanged during the electrochemical reactions originate from the materials of the intrinsic *in situ* XRD cell such as the Cu foil. We confirmed the phase changes of bismuth mainly by observing the changes in peaks in the 2θ range of 20°–30°. During the lithiation process, two steps of phase transition were identified in CV, which are in good agreement with the *in situ* XRD results, where

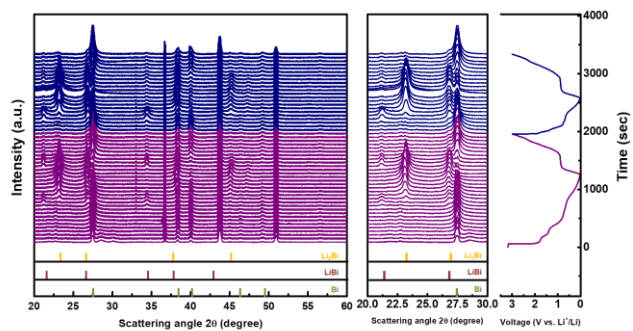


Figure 3.3.13 *In situ* XRD patterns (left side) with voltage profiles (right side) of Bi@C and enlarged XRD patterns (center) between 20 and 30 degrees

LiBi and Li₃Bi peaks were observed. In the first step, the peak intensity of the Bi metal slowly declined and the peaks of LiBi emerged simultaneously. As further electrochemical alloying took place, the LiBi peak disappeared and the Li₃Bi peak appeared, while the Bi metal peak disappeared completely at the end of the first cycle. The results indicate that the bismuth nanoparticles in the Bi@C are fully lithiated after the lithiation process. On the other hand, as shown in CV results, there is only one broad oxidation peak at ~0.93 V during the dealloying reaction. It can be considered that the lithium ion is dealloyed in a single reaction or a combination of reverse reactions of (1) and (2), simultaneously. The phase transition appears at 0.93 V during the delithiation process, and this phenomenon is consistent with the oxidation peak of the CV curve. However, it was confirmed that not only the LiBi phase but also the Bi metal phase were generated simultaneously. In particular, after 1670 s, at the end of the voltage plateau, the peak of Li₃Bi almost disappeared and the peak of LiBi also disappeared, while the intensity of the Bi metal peak increased significantly at the same time. These results indicate that the reverse reactions of (1) and (2) occur almost simultaneously during the delithiation process.

In Figure 3.3.14.a, the cycle performance test shows a capacity of ~200 mAh g⁻¹ over 1000 cycles at a current density of 3000 mA g⁻¹ for Bi@C. Both Bi@C and Bi commercial show steep capacity fading during the first several cycles due to pulverization upon cycling resulting in electrochemically inactive part at harsh conditions of current density.⁷⁶ Even though both of two samples suffer abrupt capacity fading, Bi@C shows superior capacity retention. Bi nanoparticles encapsulated in a thin layer of carbon shell are extremely advantageous as anodes because they not only have a high capacity but also boost the cell performance at high-speed charging and discharging process due to the extremely short diffusion pathway for lithium in the Bi structure. Comparison of the voltage profiles of Bi@C and commercial Bi in Figure 3.3.14.b and c indicates that Bi@C shows no potential drop even at 3000 mA g⁻¹. The hierarchically porous structure leads to fast lithiation

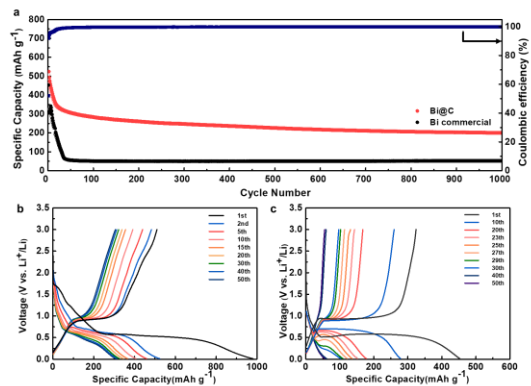


Figure 3.3.14 Cycle performance of the Bi@C and Bi commercial (a) Cycle performance at a current density of 3000 mA g⁻¹. Charge and discharge potential curves of (b) Bi@C (c) Bi commercial at a current density of 3000 mA g⁻¹

and delithiation processes, indicating that the interior part of the electrode is fully wetted. Moreover, the carbon shell increases the electrical conductivity to prevent the voltage drop.

To better understand the effect of the carbon shell on the Bi nanoparticles, EIS was conducted. The Nyquist plots in Figure 3.3.15 were obtained after 100 cycles in the frequency range of 0.01 Hz to 100 kHz. The plots of charge transfer resistance, which are semicircles located in the high frequency range, show that the charge transfer resistance of Bi@C derived from the MOFs is lower than that of a commercial Bi anode. This is because the particle size is reduced to nanoscale, which makes the diffusion length of the Li^+ ions shorter than that in micro-sized commercial Bi particles. In addition, the amorphous carbon layer effectively improves the electrical conductivity and suppresses the volume expansion of the anode. Therefore, the nanosized-Bi and amorphous carbon layer in Bi@C enhance the Li^+ diffusion rate and electrical conductivity, and suppress the volume expansion, leading to the excellent electrochemical performance of the LIB.

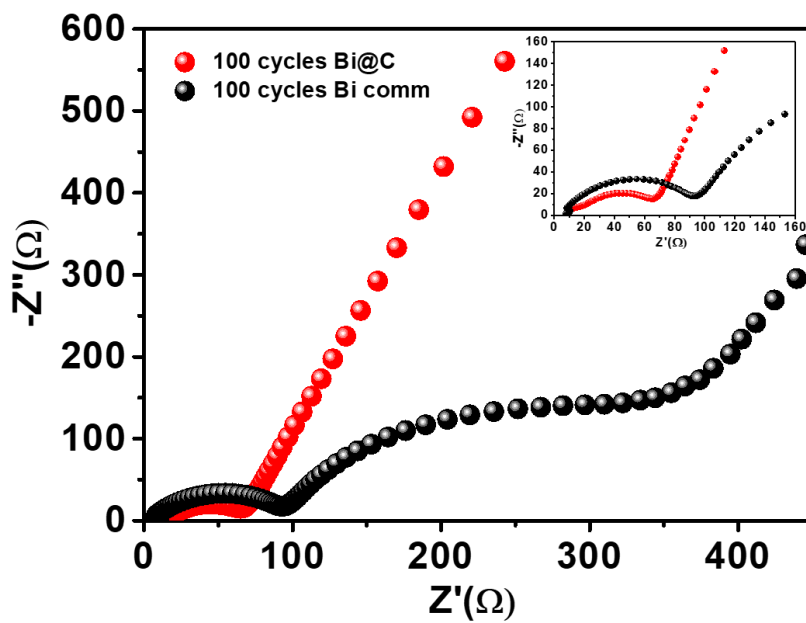


Figure 3.3.15 EIS analysis of Bi@C and Bi commercial measured after 100 cycles

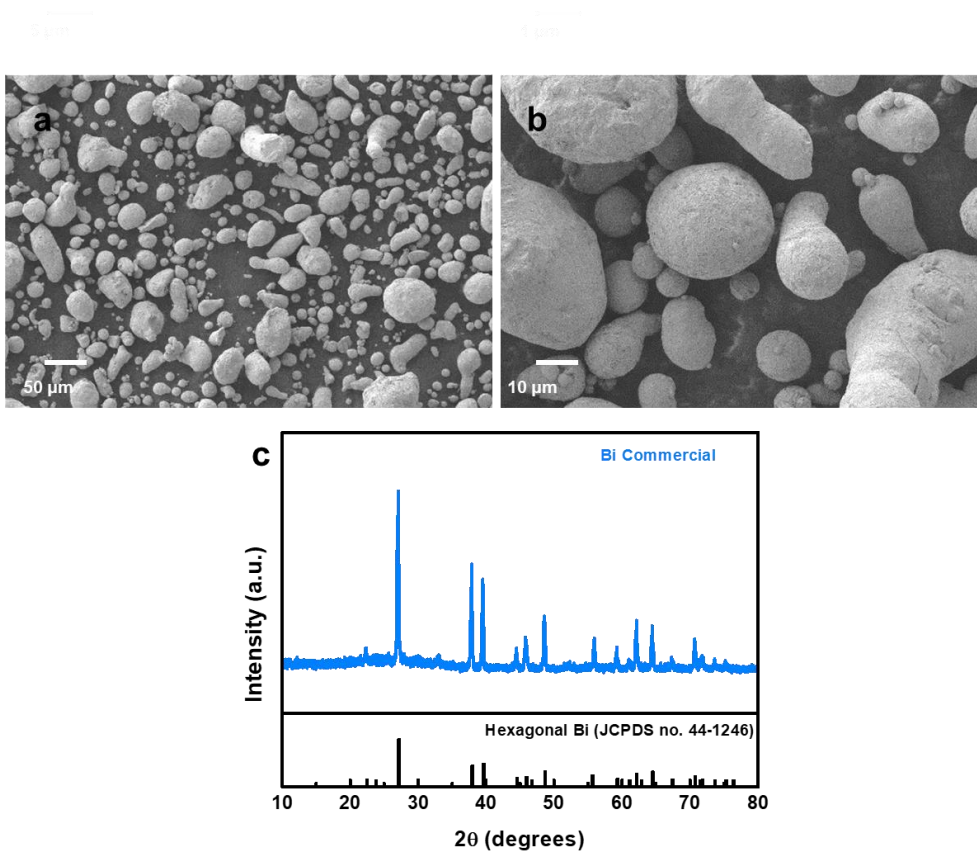


Figure 3.3.16 (a, b) SEM images and (c) XRD patterns of Bi commercial

3.4. Conclusion

In summary, we demonstrated materials composed of Bi nanoparticles enclosed in an amorphous carbon matrix with excellent volumetric capacity. The Bi@C composite was synthesized by the pyrolysis of MOFs prepared by a microwave-assisted hydrothermal method. Bi@C is composed of ~10–50 nm Bi nanoparticles in an amorphous carbon shell. The anode composed of Bi nanoparticles and amorphous carbon exhibits high capacity (556 mAh g⁻¹ after 100 cycles at 100 mA g⁻¹) and good cycling performance. Moreover, the Bi@C anode shows good performance at high current density, and excellent cyclic stability (308 mAh g⁻¹ after 50 cycles and 200 mAh g⁻¹ after 1000 cycles at 3000 mA g⁻¹). The excellent cell performance of LIBs with Bi@C anode seems to be due to the nanosized Bi and amorphous carbon shell. The nanosized Bi formed from simple heat-treatment reduces the diffusion length of Li ion, enabling high rate performance. Meanwhile, the outer shell composed of amorphous carbon suppresses pulverization and aggregation of the metal during cycling. Moreover, the carbon shell increases the electrical conductivity of the electrode, thus improving its electrochemical properties. The proposed hierarchical micro/meso-porous materials derived from MOFs are a new type of nanostructures that are promising for the development of Bi and Bi-based compounds for LIBs.

3.5. References

- (1) Armand, J.; Tarascon, J.-M. Building Better Batteries *Nature* **2008**, *451*, 652-657.
- (2) Scrosati, B.; Hassoun, J.; Sun, Y.-K. Lithium-Ion Batteries. A Look into the Future. *Energy Environ. Sci.* **2011**, *4*, 3287-3295.
- (3) Nitta, N.; Wu, F.; Lee, J. T.; Yushin, G. Li-Ion Battery Materials: Present and Future. *Mater. Today* **2015**, *18*, 252-264.
- (4) Li, X.; Wang, C. Engineering Nanostructured Anodes via Electrostatic Spray Deposition for High Performance Lithium Ion Battery Application. *J. Mater. Chem. A* **2013**, *1*, 165-182.
- (5) Thackeray, M. M.; Wolverton, C.; Isaacs, E. D. Electrical Energy Storage for Transportation-Approaching the Limits of, and Going beyond, Lithium-Ion Batteries. *Energy Environ. Sci.* **2012**, *5*, 7854-7863.
- (6) Tang, Y.; Zhang, Y.; Li, W.; Ma, B.; Chen, X. Rational Material Design for Ultrafast Rechargeable Lithium-Ion Batteries. *Chem. Soc. Rev.* **2015**, *44*, 5926-5940.
- (7) Etacheri, V.; Marom, R.; Elazari, R.; Salitra, G.; Aurbach, D. Challenges in the Development of Advanced Li-Ion Batteries: A Review. *Energy Environ. Sci.* **2011**, *4*, 3243-3262.
- (8) Dunn, B.; Kamath, H.; Tarascon, J.-M. Electrical Energy Storage for the Grid: A Battery of Choices. *Science* **2011**, *334*, 928-935.
- (9) Cabana, B. J.; Monconduit, L.; Larcher, D.; Palacin, M. R. Beyond Intercalation-Based Li-Ion Batteries: The State of the Art and Challenges of Electrode Materials Reacting through Conversion Reactions. *Adv. Mater.* **2010**, *22*, E170-192.
- (10) Manthiram, A. Materials Challenges and Opportunities of Lithium Ion Batteries. *J. Phys. Chem. Lett.* **2011**, *2*, 176-184.

- (11) Tarascon, J.-M.; Armand, M. Issues and Challenges Facing Rechargeable Lithium Batteries. *Nature* **2001**, *414*, 359.
- (12) Reddy, M. V.; Subba Rao, G. V.; Chowdari, B. V. R. Metal Oxides and Oxysalts as Anode Materials for Li Ion Batteries. *Chem. Rev.* **2013**, *113*, 5364-5457.
- (13) Kaskhedikar, B. N. A.; Maier, J. Lithium Storage in Carbon Nanostructures. *Adv. Mater.* **2009**, *21*, 2664-2680.
- (14) Poizot, P.; Laruelle, S.; Grugeon, S.; Dupont, L.; Tarascon, J.-M. Nano-Sized Transition-Metal Oxides as Negative-Electrode Materials for Lithium-Ion Batteries. *Nature* **2000**, *407*, 496-499.
- (15) Bruce, P. G.; Scrosati, B.; Tarascon, J.-M. Nanomaterials for Rechargeable Lithium Batteries. *Angew. Chem. Int. Ed.* **2008**, *47*, 2930-2946.
- (16) Yao, Y.; McDowell, M. T.; Ryu, I.; Wu, H.; Liu, N.; Hu, L.; Nix, W. D.; Cui, Y. Interconnected Silicon Hollow Nanospheres for Lithium-Ion Battery Anodes with Long Cycle Life. *Nano Lett.* **2011**, *11*, 2949-2954.
- (17) Hu, L.; Zhong, H.; Zheng, X.; Huang, Y.; Zhang, P.; Chen, W. CoMn₂O₄ Spinel Hierarchical Microspheres Assembled with Porous Nanosheets as Stable Anodes for Lithium-Ion Batteries. *Sci. Rep.* **2012**, *986*, 1-8.
- (18) Tian, X.; Gao, Q.; Zhang, H.; Li, Z.; Li, Z.; Xiao, H.; Zhang, Q.; Ma, L. Uniform small-sized MoS₂ from Novel Solution-Based Microwave-Assisted Method with Exceptional Reversible Lithium Storage Properties. *Nanoscale* **2018**, *10*, 15222-15228.
- (19) Zhang, W. -M.; Hu, J. -S.; Guo, Y. -G.; Zheng, S.- F.; Zhong, L. -S.; Song, W. -G.; Wan, L. -J. Tin-Nanoparticles Encapsulated in Elastic Hollow Carbon Spheres for High-Performance Anode Material in Lithium-Ion Batteries. *Adv. Mater.* **2008**, *20*, 1160-1165.
- (20) Li, J.; Hou, Y.; Gao, X.; Guan, D.; Xie, Y.; Chen, J.; Yuan, C.; A Three-

Dimensionally Interconnected Carbon Nanotube/Layered MoS₂ Nanohybrid Network for Lithium Ion Battery Anode with Superior Rate Capacity and Long-Cycle-Life. *Nano Energy* **2015**, *16*, 10-18.

(21) Xin, X.; Zhou, X.; Wang, F.; Yao, X.; Xu, X.; Zhu, Y.; Liu, Z. A 3D Porous Architecture of Si/Graphene Nanocomposite as High-Performance Anode Materials for LI-Ion Batteries. *J. Mater. Chem.* **2012**, *22*, 7724-7730.

(22) Magasinski, A.; Dixon, P.; Hertzberg, B.; Kvit, A.; Ayala, J.; Yushin, G.; High-Performance Lithium-Ion Anodes Using a Hierarchical Bottom-Up Approach. *Nat. Mater.* **2010**, *9*, 353-358.

(23) Liu, L.; Xie, F.; Lyu, J.; Zhao, T.; Li, T.; Choi, B. G. Tin-Based Anode Materials with Well-Designed Architectures for Next-Generation Lithium-Ion Batteries. *J. Power Sources* **2016**, *321*, 11-35.

(24) Zhu, J.; Sun, T.; Chen, J.; Shi, W.; Zhang, X.; Lou, X.; Mhaisalkar, S.; Hng, H. H.; Boey, F.; Ma, J.; Yan, Q. Controlled Synthesis of Sb Nanostructures and Their conversion to CoSb₃ nanoparticle Chains for Li-Ion Battery Electrodes. *Chem. Mater.* **2010**, *22*, 5333-5339.

(25) Hou, H.; Jing, M.; Yang, Y.; Zhu, Y.; Fang, L.; Song, W.; Pan, C.; Yang, X.; Ji, X. Sodium/Lithium Storage Behavior of Antimony Hollow Nanospheres for Rechargeable Batteries. *ACS Appl. Mater. Interfaces* **2014**, *6*, 16189-16196.

(26) Chan, C. -K.; Zhang, X. F.; Cui, Y. High Capacity Li Ion Battery Anodes Using Ge Nanowires. *Nano Lett.* **2008**, *8*, 307-309.

(27) Xue, L.; Xu, G.; Li, Y.; Li, S.; Fu, K.; Shi, Q.; Zhang, X. Carbon-Coated Si Nanoparticles Dispersed in Carbon Nanotube Networks as Anode Material for Lithium-Ion Batteries. *ACS Appl. Mater. Interfaces* **2013**, *5*, 21-25.

(28) Park, C. -M.; Yoon, S.; Lee, S. -I.; Sohn, H. -J. Enhanced Electrochemical Properties of Nanostructured Bismuth-Based Composites for Rechargeable Lithium

Batteries. *J. Power Sources* **2009**, *186*, 206-210.

(29) Finke, A.; Poizot, P.; Guery, C.; Dupont, L.; Taberna, P. -L.; Simon, P.; Tarascon, J. -M. Electrochemical Method for Direct Deposition of Nanometric bismuth and Its Electrochemical Properties vs Li. *Electrochemical. Solid. St.* **2008**, *11*, E5-E9.

(30) Lan, J. -L.; Jin, Y.; Qin, C.; Yu, Y.; Yang, X. Bio-Inspired Rose-Like Bi@Nitrogen-Enriched Carbon towards High-Performance Lithium-Ion Batteries. *ChemistrySelect* **2017**, *2*, 7178-7184.

(31) Kim, M. -K.; Yu, S. -H.; Jin, A.; Kim, J.; Ko, I. -H.; Lee, K. -S.; Mun, J.; Sung, Y. -E. Bismuth Oxide as a High Capacity Anode Material for Sodium-Ion Batteries. *Chem. Commun.* **2016**, *52*, 11775-11778.

(32) Zhang, Y.; Wang, Q.; Wang, B.; Mei, Y.; Lian, P. N-Doped Graphene/Bi Nanocomposite with Excellent Electrochemical Properties for Lithium-Ion Batteries. *Ionics* **2017**, *23*, 1407-1415.

(33) Li, Y.; Trujillo, M. A.; Fu, E.; Patterson, B.; Fei, L.; Xu, Y.; Deng, S.; Smirnov, S.; Luo, H. Bismuth Oxide : a New Lithium-Ion Battery Anode. *J. Mater. Chem. A* **2013**, *1*, 12123-12127.

(34) Yin, H.; Cao, M. -L.; Yu, X. -X.; Zhao, H.; Shen, Y.; Li, C.; Zhu, M. -Q. Self-Standing Bi₂O₃ Nanoparticles/Carbon Nanofiber Hybrid Films as a Binder-Free Anode for Flexible Sodium-Ion Batteries. *Mater. Chem. Front.* **2017**, *1*, 1615-1621.

(35) Zheng, H.; Li, H.; Yu, M.; Zhang, M.; Tong, Y.; Cheng, F.; Lu, X. Vertical Bismuth Oxide Nanosheets with Enhanced Crystallinity : Promising Stable Anodes for Rechargeable Alkaline Batteries. *J. Mater. Chem. A* **2017**, *5*, 25539-25544.

(36) Luo, W.; Li, F.; Li, Q.; Wang, X.; Yang, W.; Zhou, L.; Mai, L. Heterostructured Bi₂S₃-Bi₂O₃ Nanosheets with a Built-In Electric Field for Improved Sodium Storage. *ACS Appl. Mater. Interfaces* **2018**, *10*, 7201-7207.

(37) Dawei, S.; Dou, S.; Wang, G. Bismuth : A New Anode for the Na-Ion Battery.

Nano Energy **2015**, *12*, 88-95.

(38) Dai, R.; Wang, Y.; Da, P.; Xu, M.; Zheng, G. Indirect Growth of Mesoporous Bi@C Core-Shell Nanowires for Enhanced Lithium-Ion Storage. *Nanoscale* **2014**, *6*, 13236-13241.

(39) Xianming, W.; Nishina, T.; Uchida, I. Lithium Alloy Formation at Bismuth Thin Layer Electrode and its Kinetics in Propylene Carbonate Electrolyte. *J. Power Sources* **2002**, *104*, 90-96.

(40) Nitta, N.; Yushin, G. High-Capacity Anode Materials for Lithium-Ion Batteries : Choice of Elements and Structures for Active Particles. *Part. Part. Syst. Charact.* **2014**, *31*, 317-336.

(41) Crosnier, O.; Devaux, X.; Brousse, T.; Fragnaud, P.; Schleich, D. M. Influence of Particle Size and Matrix in “metal” Anodes for Li-Ion Cells. *J. Power Sources* **2001**, *97-98*, 188-190.

(42) Obrovac, M. N.; Chevrier, V. L. Alloy Negative Electrodes for Li-Ion Batteries. *Chem. Rev.* **2014**, *114*, 11444-11502.

(43) Ko, M.; Chae, S.; Cho, J. Challenges in Accommodating Volume Change of Si Anodes for Li-Ion batteries. *ChemElectroChem.* **2015**, *2*, 1645-1651.

(44) Yaghi, O. M.; Li, H. Hydrothermal Synthesis of a Metal-Organic Framework Containing Large Rectangular Channels. *J. Am. Chem. Soc.* **1995**, *117*, 10401-10402.

(45) Farha, O. K.; Eryazici, I.; Jeong, N. C.; Hauser, B. G.; Wilmer, C. E.; Sarjeant, A. A.; Snurr, R. Q.; Nguyen, S. T.; Yazaydin, A. O.; Hupp, J. T. Metal-Organic Framework Materials with Ultrahigh Surface Areas : Is the Sky the Limit? *J. Am. Chem. Soc.* **2012**, *134*, 15016-15021.

(46) Furukawa, H.; Cordova, K. E.; O’Keeffe, M.; Yaghi, O. M. The Chemistry and Applications of Metal-Organic Frameworks. *Science* **2013**, *341*, 1230444.

(47) Lee, J. Y.; Roberts, J. M.; Farha, O. K.; Sarjeant, A. A.; Scheidt, K. A.; Hupp, J.

T. Synthesis and Gas Sorption Properties of a Metal-Azolium Framework (MAF) Material. *Inorg. Chem.* **2009**, *48*, 9971-9973.

(48) Corma, A.; Garcia, H.; Xamena, F. X. L. Engineering Metal Organic Frameworks for Heterogeneous Catalysis *Chem. Rev.* **2010**, *110*, 4606-4655.

(49) Alaerts, L.; Seguin, E.; Poelman, H.; Thibault-Starzyk, F.; Jacobs, P. A.; De Vos, D. E. Probing the Lewis Acidity and Catalytic Activity of the Metal-Organic Framework [Cu₃(btc)₃] (BTC = Benzene-1,3,5- tricarboxylate) *Chem. Eur. J.* **2006**, *12*, 7353-7363.

(50) Qamar, M.; Adam, A.; Merzougui, B.; Helal, A.; Abdulhamid, O. Siddiqui, M. N. Metal-Organic Framework-Guided Growth of Mo₂C embedded in Mesoporous Carbon as a High-Performance and Stable Electrocatalyst for the Hydrogen Evolution Reaction. *J. Mater. Chem. A* **2016**, *4*, 16225-16232.

(51) Shen, L.; Wu, W.; Liang, R.; Lin, R.; Wu, L. Highly Dispersed Palladium Nanoparticles Anchored on UiO-66(NH₂) Metal-Organic Framework as a reusable and Dual Functional Visible-Light-Driven Photocatalyst *Nanoscale* **2013**, *5*, 9374-9382.

(52) Ryu, S. G.; Kim, M. -K.; Park, M.; Jang, S. O.; Kim, H.; Jung, H. Availability of Zr-Based MOFs for the Degradation of Nerve Agents in All Humidity Conditions. *Micropor. Mesopor.* **2019**, *274*, 9-16.

(53) Sun, C. -Y.; Liu, S. -X.; Liang, D. -D.; Shao, K. -Z.; Ren, Y. -H.; Su, Z. -M. Highly Stable Crystalline Catalysts Based on a Microporous Metal-Organic Framework and Polyoxometalates. *J. Am. Chem. Soc.* **2009**, *131*, 1883-1888.

(54) Rosi, N. L.; Eckert, J.; Eddaoudi, M.; Vodak, D. T.; Kim, J.; O'Keeffe, M.; Yaghi, O. M. Hydrogen Storage in Microporous Metal-Organic Frameworks. *Science* **2003**, *300*, 1127-1129.

(55) Li, S.; Huw, F. Metal-Organic Framework Composites : from Fundamentals to

Applications. *Nanoscale* **2015**, *7*, 7482-7501.

(56) Ricco, R.; Malfatti, L.; Takahashi, M.; Hill, A. J.; Falcaro, P. Applications of Magnetic Metal-Organic Framework Composites. *J. Mater. Chem. A*. **2013**, *1*, 13033-13045.

(57) Xie, J.; Zhu, Y.; Zhuang, N.; Lei, H.; Zhu, W.; Fu, Y.; Javed, M. S.; Li, J.; Mai, W. Rational Design of Metal Organic Framework-Derived FeS₂ Hollow Nanocages@Reduced Graphene Oxide for K-Ion Storage. *Nanoscale* **2018**, *10*, 17092-17098.

(58) Morozan, A.; Jaouen, F. Metal Organic frameworks for Electrochemical Applications. *Energy Environ. Sci.* **2012**, *5*, 9269-9290.

(59) Li, S. -L; Xu, Q. Metal-Organic Frameworks as Platforms for Clean Energy. *Energy Environ. Sci.* **2013**, *6*, 1656-1683.

(60) Wang, Lu.; Han, Y.; Feng, X.; Zhou, J.; Qi, P.; Wang, B. Metal-Organic frameworks for Energy Storage : Batteries and Supercapacitors. *Coord. Chem. Rev.* **2016**, *307*, 361-381.

(61) Zhao, S.; Wang, Y.; Dong, J.; He, C. -T.; Yin, H.; An, P.; Zhao, K.; Zhang, X.; Gao, C.; Zhang, L.; Lv, J.; Wang, J.; Zhang, J.; Khattak, A. M.; Khan, N. A.; Wei, Z.; Zhang, J.; Liu, S.; Zhao, H.; Tang, Z. Ultrathin Metal-Organic Framework Nanosheets for Electrocatalytic Oxygen Evolution. *Nat. Energy* **2016**, *1*, 16184.

(62) Wu, H. B.; Wei, S.; Zhang, L.; Xu, R.; Hng, H. H.; Lou, X. W. Embedding Sulfur in MOF-Derived Microporous Carbon Polyhedrons for Lithium-Sulfur Batteries. *Chem. Eur. J.* **2013**, *19*, 10804-10808.

(63) Wang, G.; Liu, Y.; Huang, B.; Qin, X.; Zhang, X.; Dai, Y. A Novel Metal-Organic Framework Based on Bismuth and Trimesic Acid : Synthesis, Structure and Properties. *Dalton Trans.* **2015**, *44*, 16238-16241.

(64) McNulty, D.; Geaney, H.; Armstrong, E.; O'Dwyer, C. High Performance

Inverse Opal Li-Ion Battery with Paired Intercalation and Conversion Mode Electrodes. *J. Mater. Chem. A* **2016**, *4*, 4448-4456.

(65) Zhou, Y.; Rui, X.; Sun, W.; Xu, Z.; Zhou, Y.; Ng, W. J.; Yan, Q.; Fong, E. Biochemistry-Enabled 3D Foams for Ultrafast Battery Cathodes. *ACS Nano* **2015**, *9*, 4628-4635.

(66) Hardy, A.; Gielis, S.; Van den Rul, H.; D'Haen, J.; Van Bael, M. K.; Mullens, J. Effects of Precursor Chemistry and Thermal treatment Conditions on Obtaining Phase Pure Bismuth Ferrite from Aqueous Gel Precursors. *J. Eur. Ceram. Soc.* **2009**, *29*, 3007-3013.

(67) Zhao, S.; Yang, Z.; Jiang, W.; Kang, L.; Liu, N.; Meng, Y.; Sun, C. Sn/Carbon Nanofibers Fabricated by electrospinning with Enhanced Lithium Storage Capabilities. *RSC adv.* **2016**, *6*, 111976-111981.

(68) Crosnier, O.; Brousse, T.; Devaux, X.; Fragnaud, P.; Schleich, D. M. New Anode Systems for Lithium Ion Cells. *J. Power Sources* **2001**, *94*, 169-174.

(69) Zhang, W. -M.; Hu, J. -S.; Guo, Y. -G.; Zheng, S. -F.; Zhong, L. -S.; Song, W. -G.; Wan, L. -J. Tin-Nanoparticles Encapsulated in Elastic Hollow carbon Spheres for High-Performance Anode Material in Lithium-Ion Batteries. *Adv. Mater.* **2008**, *20*, 1160-1165.

(70) Cao, X.; Shi, Y.; Shi, W.; Rui, X.; Yan, Q.; Kong, J.; Zhang, H. Preparation of MoS₂-Coated Three-Dimensional Graphene Networks for High-Performance Anode Material in Lithium-Ion Batteries. *Small.* **2013**, *9*, 3433-3438.

(71) Li, W.; Yang, Z.; Cheng, J.; Zhong, X.; Gu, L.; Yu, Y. Germanium Nanoparticles Encapsulated in Flexible Carbon Nanofibers as Self-Supported Electrodes for High-Performance Lithium-Ion Batteries. *Nanoscale* **2014**, *6*, 4532-4537.

(72) Zhu, J.; Lei, D.; Zhang, G.; Li, Q.; Lu, B.; Wang, T. Carbon and Graphene Double Protection Strategy to Improve the SnO_x Electrode Performance Anodes for

Lithium-Ion Batteries. *Nanoscale* **2013**, *5*, 5499-5505.

(73) Role of Transition Metal Nanoparticles in the Extra Lithium Storage Capacity of Transition Metal Oxides : a Case Study of Hierarchical Core-Shell Fe₃O₄@C and Fe@C Microspheres Sodium/Lithium Storage Behavior of Antimony Hollow Nanospheres for Rechargeable Batteries. *J. Mater. Chem. A* **2013**, *1*, 15158-15166.

(74) Laruelle, S.; Grugeon, S.; Poizot, P.; Dolle, M.; Dupont, L.; Tarascon, J. -M. On the Origin of the Extra Electrochemical Capacity Displayed by MO/Li Cells at Low Potential. *J. Electrochem. Soc.* **2002**, *149*, A627-A634.

(75) Sun, C. -F.; Hu, J.; Wang, P.; Cheng, X. -Y.; Lee, S. B.; Wang, Y. Li₃PO₄ Matrix Enables a Long Cycle Life and High Energy Efficiency Bismuth-Based Battery. *Nano Lett.* **2016**, *16*, 5875-5882.

(76) Zhong, Y.; Li, B.; Li, S.; Xu, S.; Pan, Z.; Huang, Q.; Xing, L.; Wang, C.; Li, W. Bi Nanoparticles Anchored in N-Doped Porous Carbon as Anode of High Energy Density Lithium Ion Battery. *Nano-Micro Lett.* **2018**, *10*, 56.

(77) Wu, L.; Lu, H. Xiao, L.; Qian, J.; Ai, X.; Yang, H.; Cao, Y. A Tin(II) Sulfide-Carbon Anode Material Based on Combined Conversion and Alloying Reactions for Sodium-Ion Batteries *J. Mater. Chem. A* **2014**, *2*, 16424-16428.

리튬이온전지를 위한 티타늄 산화물과 비스무스 전극 물질의 메커니즘 연구

리튬이온배터리는 다른 에너지 저장 장치와 비교해서 긴 수명과 높은 에너지 밀도 때문에 전 세계에서 많은 관심을 받아오고 있다. 하지만, 현재 널리 사용 중인 흑연 음극은 낮은 이론 용량 (372 mAh g^{-1}) 과 체적용량 (840 mAh cm^{-3}) 때문에 증가된 수요를 충족하지 못한다. 이를 대체하기 위해서, 많은 대체 전극 물질에 대해서 상온 뿐만 아니라 높아진 온도에서도 연구가 되고 있다.

1 장에서는 다음 챕터들을 이해하기 쉽게하기 위해서, 리튬이온배터리의 일반적인 컨셉에 대해서 설명한다. 이어서, 더 자세하게, 티타늄 산화물의 메커니즘 연구에 대한 전체적인 연대기적 기록에 대해서 설명하고, 비스무스 메탈의 연구 트렌드에 대해서 제시한다.

2 장에서는 티타늄 산화물을 모델 물질로 사용하여, 리튬이온배터리의 온화한 열 조건에서의 화학적이고 구조적인 원인에 대해 연구했다. 리튬이온배터리는 열 발생을 수반하면서 상온보다 $20 - 40 \text{ }^\circ\text{C}$ 높은 조건에서 구동하는 경우가 많다. 열적 기여가 거시적인 관찰을 통해서 배터리 성능을 감소시킨다는 것이 확인되었지만, 온화한 열조건에서 분자레벨에서 구조적이고 화학적인 원인은 아직 명확하게 설명되지 않았다. 전기화학적 측정과, 전자현미경 및 제자리 분석의 실험을 결합하여, 이 실험에서 온화한 열조건에서의 배터리 성능에 대한 통찰력을 제공한다. 흥미롭게도, 일반적인 구동 온도에서는 관찰되지 않는 과량의 리튬 저장이 심지어 $45 \text{ }^\circ\text{C}$ 에서도 관측된다. 비정상적인 리튬 삽입이 초기에는 티타늄 산화물의 추가적인 상 변화를 가능하게 하지만, 결과적으로는 치명적인 결정 균열이 일어나고 이것이 배터리 열화과정을 일으킨다. 높은 구동 온도에서의 배터리 열화는 삽입 혼합물에서 흔하게 일어나는 현상이며, 그러므로, 보다 진보된 전극물질을 위해서는 열화과정의 원인에 대해서 이해하는 것이 중요하다.

3 장에서는 마이크로/메조 다공성 Bi@C 나노 플레이트는 Bi-MOF (금속 유기 골격체) 를 열처리한 후 마이크로 웨이브 보조 방법으로 합성하여, 리튬화/탈리튬화 과정 동안 전극 물질의 부피 팽창 및 분해를 완화 한다. Bi@C 나노플레이트는 비정질 탄소 셸에 쌓인 10 - 50 nm 크기의 비스무스 나노입자로 구성된다. 전극 재료는 100 mA g⁻¹의 전류 밀도에서 100 사이클 후 높은 비용량 (556 mAh g⁻¹) 의 우수한 사이클 성능을 나타낸다. 게다가, Bi@C 나노플레이트는 3000 mA g⁻¹의 매우 높은 전류 밀도에서도 1000 사이클 이후에 200 mAh g⁻¹을 나타내는 우수한 안정적인 성능을 나타낸다. 이러한 뛰어난 성능은, 설계된 음극이 리튬 이온의 확산 길이를 줄이고, 음극의 전기 전도도를 향상시켜며 구동과정에서 분해 및 응집을 억제하는 나노 크기의 비스무스 및 탄소 셸 덕분이다. 비스무스 금속 유기 골격체에서 파생된 계층적 마이크로/메조 다공성 물질은 리튬이온 배터리를 위한 새로운 비스무스 기반 음극을 설계하기 위한 새로운 유형의 나노구조이다.

키워드 : 리튬이온배터리, 메커니즘 스터디, 온화한 열조건, 티타늄 산화물, 비스무스, 금속 유기 골격체

학 번 : 2017-25533

List of Publication

1st or Co-1st Author

1. **Min-Seob Kim**†, Byoung-Hoon Lee†, Jae-Hyuk Park†, Hyeon Seok Lee, Wytse Hooch Antink, Euiyeon Jung, Jiheon Kim, Tae Yong Yoo, Chan Woo Lee, Chi-Yeong Ahn, Seok Mun Kang, Jinsol Bok, Wonjae Ko, Xiao Wang, Sung-Pyo Cho, Seung-Ho Yu*, Taeghwan Hyeon*, Yung-Eun Sung*, Operando Identification of the Chemical and Structural Origin of Li-Ion Battery Aging at Near-Ambient Temperature, *J. Am. Chem. Soc.* **2020**, *142*, 13406.
2. Min-Kun Kim†, **Min-Seob Kim**†, Jae-Hyuk Park, Jin Kim, Chi-Yeong Ahn, Aihua Jin, Junyoung Mun*, Yung-Eun Sung*, Bi-MOF Derived Micro/Meso-Porous Bi@C Nanoplates for High Performance Lithium-Ion Batteries, *Nanoscale*, 2020, *12*, 15214.
3. Jaewon Kim†, **Min-Seob Kim**†, Youngseok Lee, Shin-Yeong Kim, Yung-Eun Sung*, Seung Hwan Ko*, Hierarchically Structured Conductive Polymer Binders with Silver Nanowires for High-Performance Silicon Anodes in Lithium-Ion Batteries, *ACS Appl. Mater.* **2022**, *14*, 17340.
4. Yunseo Jeoun†, **Min-Seob Kim**†, Si-Hwan Lee, Ji Hyun Um, Yung-Eun Sung*, Seung-Ho Yu*, Lean-Electrolyte Lithium-Sulfur Batteries: Recent Advances in the Design of Cell Components, *Chem. Eng. J.* **2022**, *450*, 138209.

Co-Author

1. Seok Mun Kang, Duho Kim, Kug-Seung Lee, **Min-Seob Kim**, Aihua Jin, Jae-Hyuk Park, Chi-Yeong Ahn, Tae-Yeol Jeon, Young Hwa Jung, Seung-Ho Yu*, Junyoung Mun*, Yung-Eun Sung*, Structural and

Thermodynamic Understandings in Mn-Based Sodium Layered Oxides during Anionic Redox, *Adv. Sci.* **2020**, 2001263.

2. Aihua Jin, Narae Kang, Ji Hyun Um, In-Hwan Ko, **Min-Seob Kim**, Kookhan Kim, So Hee Kim, Seung-Ho Yu*, Yung-Eun Sung*, Sn (salen)-derived SnS Nanoparticles Embedded in N-doped Carbon for High Performance Lithium-Ion Battery Anodes, *Chem. Commun.* **2020**, 56, 8095.
3. Seok Mun Kang, **Min-Seob Kim**, Yunseo Jeoun, Chairul Hudaya, Yung-Eun Sung*, NaCrO₂/Coffee Waste-Derived Nitrogen-Doped Carbon Composite as High-Performance Cathode Material for Sodium Ion Batteries, *Bull. Korean Chem. Soc.* 2019, 40, 857
4. Dae-Hyeok Lee†, Byoung-Hoon Lee†, Arun K Sinha†, Jae-Hyuk Park, **Min-Seob Kim**, Jungjin Park, Heejong Shin, Kug-Seung Lee, Yung-Eun Sung*, Taeghwan Hyeon*, Engineering Titanium Dioxide Nanostructures for Enhanced Lithium-Ion Storage, *J. Am. Chem. Soc.* **2018**, 140, 16676.